UNIVERSITY OF CALIFORNIA
RIVERSIDE

Zinc Oxide Based Nonvolatile Memories and Random Lasers

A Dissertation submitted in partial satisfaction
of the requirements for the degree of

Doctor of Philosophy

in

Electrical Engineering

by

Jian Huang

December 2013

Dissertation Committee:
Dr. Jianlin Liu, Chairperson
Dr. Sheldon Tan
Dr. Elaine Haberer

The Dissertation of Jian Huang is approved:

_____

_____

_____

Committee Chairperson

University of California, Riverside

ACKNOWLEDGEMENTS

First and foremost, I would like to gratefully and sincerely thank my advisor, Prof. Jianlin Liu, for the support of my Ph.D research, and for his guidance, understanding and patience. His encouragement, sound advice and lots of valuable ideas are great help for me to achieve my research goals. I appreciate the knowledge and skills he taught me and I believe these will definitely benefit my future career.

I would also like to thank my final dissertation defense committee members, Dr. Tan and Dr. Haberer, for their time, insightful questions and helpful comments.

I want to thank Dr. Dong Yan and my labmates Dr. Jing Qi, Dr. Jingjian Ren, Dr. Sheng Chu, Dr. Zheng ZuO, Dr. Guoping Wang, Dr. Jieying Kong, Ms Zonglin Li, Dr. Lin Li, Mr. Mario Olmedo, Dr. Ning Zhan, Dr. Bei Li, Dr. Huimei Zhou, Mr. Monzur Morshed, Mr. Zhongguang Xu, Ms. Renjing Zheng and others who gave me help during my PhD research and study.

Finally, I must express my very profound gratitude to my parents and my wife. Their encouragement and support make this dissertation possible. I cannot thank you enough.

This thesis is dedicated to my wife and daughter.

ABSTRACT OF THE DISSERTATION

Zinc Oxide Based Nonvolatile Memories and Random Lasers

by

Jian Huang

Doctor of Philosophy, Graduate Program in Electrical Engineering
University of California, Riverside, December 2013
Dr. Jianlin Liu, Chairperson

Nonvolatile memory devices and random laser devices based on ZnO thin film and nanostructures are studied and discussed in this dissertation. The p-n-p nonvolatile memory was achieved by using Sb-ZnO/ZnO/Sb-ZnO structure in Chapter 2. Secondary ion mass spectrometry result confirmed the formation of the structure. Rectifying current-voltage characteristics between Sb-ZnO and undoped ZnO layers were achieved, proving the p-n junction was formed. The p-type behavior from the p-n-p structure was studied by using the capacitance-voltage measurement and small signal model. The voltage operation led to the charging/discharging of the structure, showing nonvolatile memory effect. Low writing voltage and long retention time were achieved. The n-p-n nonvolatile memory based on Na-doped ZnO nanostructures was also studied in Chapter 3. To achieve n-p-n nonvolatile memory, the Na-doped nanorods were grown on a ZnO seed layer on Si. The p-type conductivity of the Na-doped nanorods was studied by temperature-dependent photoluminescence and nanorod back-gated field effect transistor. Vertically aligned undoped ZnO nanotips, nanotubes and nanorods were synthesized on

the top facets of Na-doped ZnO nanorods without catalytic assistance under different growth time in a chemical vapor deposition system. The undoped nanorods, Na-doped nanorods and undoped seed layer form an n-p-n memory structure. The programming and retention characteristics have been demonstrated. Furthermore, the bipolar resistive switching memory using Na-doped ZnO nanowire was also demonstrated in Chapter 4. The mechanism of the self-complianced and self-rectifying effect of the device was studied.

The ZnO based optoelectronics devices are studied in Chapter 5 and 6. An electrically pumped ZnO homojunction random laser diode based on nitrogen doped p-type ZnO nanowires was achieved. The p-type behaviors were studied by output characteristic and transfer characteristic of the nanowire back-gated field effect transistor, as well as low-temperature photoluminescence. The formation of the p-n junction is confirmed by the current-voltage characteristic and electron-beam-induced current. The random lasing behaviors were demonstrated by using both optical pumping and electrical pumping, with a threshold of 300 kW/cm^2 and 40 mA, respectively. The angle dependant electroluminescence of the device further proved the random lasing mechanism. To enhance the output power and reduce the threshold current of the random laser, a 10-period SiO_2/SiN_x distributed Bragg reflector (DBR) was introduced into the device. The formation of the homojunction p-n junction was confirmed by the current-voltage and photocurrent characteristics. The random lasing behaviors were demonstrated by electrical pumping with a low threshold of around 3 mA. The output power was measured to be 220 nW at 16 mA drive current.

Table of Contents

List of Figures

List of Tables

Chapter 1

Introduction

1.1 Properties of ZnO

ZnO, as an inorganic compound, has been widely used in industry and our daily life. There are three different crystal structures of ZnO: zinc blende, wurtzite, and rocksalt [1]. Under normal ambient condition, ZnO normally forms the wurtzite (Figure 1.1) structure with lattice constant of a = 0.325 nm and c = 0.512 nm. The ZnO discussed in this dissertation is wurtzite structure ZnO unless otherwise noted.

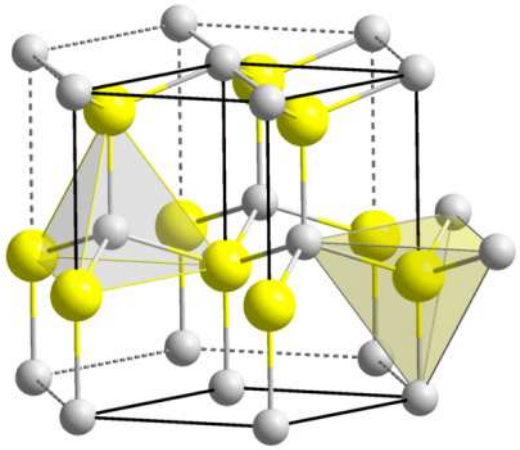

Figure 1.1. Schematic of wurtzite structure. (Source: wikipedia.org)

As II-VI semiconductor, ZnO has a band gap of 3.37 eV at room temperature, which makes it a promising candidate for ultraviolet (UV) optoelectronic devices and wide band gap nonvolatile memory devices. Its wide band gap can significantly reduce

the generation related leakage current of a nonvolatile memory and thus improve the retention performance of the device [2]. As a direct band gap semiconductor, ZnO can be ideal material for light emitting diode (LED) and laser diode (LD). Its large exciton binding energy of 60 meV [3] at room temperature enables the possibility of low threshold semiconductor laser diode. Its alloys $Zn_{(1-x)}Mg_xO$ with larger band gap and $Zn_{(1-y)}Cd_yO$ with smaller band gap can be formed while alloying ZnO with MgO or CdO, respectively [4]. Furthermore, ZnO can be synthesized with low cost using different mature technology such as MBE, CVD and PLD. The 2-dimensional thin film can be achieved on both sapphire and silicon [5,6], which is critical for microelectronics applications. Besides, diverse nanostructures of ZnO can be controllably achieved by different methods [7].

For many optoelectronics and microelectronics devices, both n-type and p-type materials are needed. However, due to the “intrinsic” donors such as zinc interstitials and oxygen vacancies [8, 9] and the unintentional donor hydrogen [10], ZnO is an “intrinsic” n-type material. Reliable p-type conductivity is difficult to achieve, which poses the largest obstacle on the application of ZnO. The group I and group V elements are typically considered to be p-type dopants for ZnO and a great deal of efforts have been made to achieve the p-type conductivity.

Among the group I dopants (Li, Na, K), the element Na can substitute for Zn and has a shallow acceptor level of 170 meV in theory [11]. In experiment, p-type ZnO thin films doped with Na have been fabricated on quartz and glass with hole concentrations up to 3×10^{18} cm^{-3} [12]. For one dimensional structure, there have been few reports on p-

type ZnO doped with Na [13, 14]. In ref [13], the typical length of these randomly distributed microwires is found to be several hundred micrometers and the diameters of most of the microwires are in the range 2-6 μm, which is not possible to be used for nanoelectronic devices. In ref [14], the p-type conductivity is not clear from the very low on/off ratio FET. In other words, Na doped p-type ZnO nanowires, which can be used to fabricate nanoscale devices, still need to be further studied.

The group V element Sb can also introduce acceptor into ZnO. Based on first-principle calculations, antimony (Sb) can produce shallow acceptor levels in ZnO if Sb atom substitutes Zn atom and connects with two Zn vacancies [15]. Experimentally, Sb doped p-type ZnO thin films and nanowires have been reported by different groups. Xiu et al reported p-type Sb doped ZnO thin film with hole concentration of 1.7×10^{18} cm^{-3} and high mobility of 20.0 cm^2/Vs [16]. Aoki et al. reported Sb-doped p-type ZnO thin film with a hole mobility of 1.5 cm^2/Vs and an acceptor concentration of $5\times10^{20}cm^{-3}$ [17]. For nanowires, stable Sb doped nanowires with field effect mobility of 0.7 cm^2/Vs and hole concentration of 1.2×10^{17} cm^{-3} has been reported recently [18]. Various optoelectronic devices based on Sb doped p-type ZnO such as photodetectors [19], light emitting diodes [20] and nanowire lasing devices [21] have been developed. These devices further confirm the p-type conductivity of the p-type Sb doped ZnO.

Nitrogen, which has a similar atomic radius with oxygen, has also been reported to be a good p-type dopant for ZnO [22-24] in experiments. Although nitrogen substitution of lattice oxygen (N_O) will form an acceptor level in ZnO, the activation energy of the acceptor is still disputed. Park et al suggested that the activation energy is

about 0.4 eV based on density functional theory [25] while Li et al got a value of 0.31 eV using first-principles band-structure calculations [26]. Both calculations show that nitrogen is shallow acceptor and p-type nitrogen doped ZnO can be achieved at room temperature. However, a study from Lyons et al predicted that N_O may not produce p-type ZnO at all with an activation energy of 1.3 eV [27]. Then the fact that nitrogen doped ZnO shows p-type becomes intriguing for researchers. Recently, Liu et al reported that a nitrogen related defect complex N_O-V_{Zn} will have a shallow acceptor activation energy of 0.23 meV and this complex can be formed under Zn-polar growth condition [28]. This research opens a new window for the nitrogen doping of ZnO.

1.2 Motivation of the ZnO based device research

Flash memories are currently widely used for semi-permanent data storage such as PDAs (personal digital assistants), laptop computers, digital audio players, digital cameras and mobile phones. Storage time of these memories is measured to be around 10 years, but the writing operation is quite slow comparing with RAM, typically on the order of micro second per bit. In addition, they all suffer from a wear-out mechanism that limits the number of times the memory can be reprogrammed to around 10^5 times (Table 1.2).

Characteristics	**Detail**
Program voltage:	NOR: 7-9V NAND: 17-19V
Program speed:	NOR: 1 μs/bit NAND: 1 ms/page
Endurance:	~10^5 times
Retention:	<10 years

Table 1.1. Parameters for flash memory.

The flash memory still can satisfy most device requirements, nevertheless, to overcome the shortcomings of the flash memory and achieve next generation memory, other members of nonvolatile memory family, such as Ferroelectric RAM (FRAM) Magnetic RAM (MRAM), Phase-change RAM (PRAM), organic memory and Resistive RAM (ReRAM), have attracted much attention. Among so many types of nonvolatile memories, each one has its own advantages and disadvantages. The main advantage of FeRAM is the low power consumption. However, because the readout method of FeRAM is destructive (the bit information will be destroyed if it is read), the maximum number of readouts is limited. Furthermore, FeRAM is difficult to achieve high-density integration because of its capacitor-type memory cell [29]. For MRAM, the high operating speed

which can be equivalent to that of SRAM is the most outstanding feature. But present MRAM needs large current to program and because of its complicated structure it is not suitable to achieve high-density integration now [30]. PRAM has a simple structure and is considered to be suitable for high-density integration. And it can achieve million-year retention time and high program speed. However, in practical use, operating this kind of memory needs a large current (usually exceed 10^{-5} A) [31]. This will require the high current drivability cell-selection transistor for the circuit, which makes the miniaturization of transistors difficult. The organic memory usually can achieve their function by using a single molecule which means it can be easily scaled down. However this kind of molecule is usually not able to survive in the heat during the device fabrication.

In 1990s, some researchers reported a prototype nonvolatile random access memory: a high-speed read-write memory based on 6H silicon carbide (6H-SiC) p-n-p/n-p-n structures [32-34]. This nonvolatile RAM does not suffer from the wear-out mechanism and therefore even can be used in applications which are normally served by dynamic RAM. Besides, it achieved low operation voltage due to diode operation and thousands of years' retention time due to low thermal generation rate from wide band gap. But the problem lies in how to get low cost and the high quality wide band gap materials.

High quality ZnO thin film and nanowires can be grown on different substrate. This will reduce the material cost of this memory if ZnO is used instead of SiC.

Furthermore, ZnO has a larger band gap which can further improve the performance of the devices.

ReRAM could be another hopeful candidate of new generation memory for its simple structure and fast speed [35]. It is thought to be an ideal nonvolatile memory after the 22 nm technology node. But the mechanism of this memory is not clear yet and needs to be understood. Several problems such as insufficient retention time and endurance performance still need to be solved. ZnO is promising material for ReRAM due to its unique properties. First, ZnO based ReRAM has both unipolar and bipolar resistive switching behaviors [36,37], which make it excellent material for resistive switching mechanism study. Second, ZnO based ReRAM has been reported to have the larger high resistance to low resistance ratio and long retention time [38]. Third, various dopants can be introduced into ZnO to improve the ReRAM performance [39,40]. Furthermore, its ease of growth and low synthesis cost make it a more competitive candidate for further applications.

Another important application of ZnO is for optoelectronic device. According to 2010 Optoelectronics Market Report by Databeans, Inc., the market of optoelectronics will reach $36.5 billion by 2015, sharing about 9 percent of the semiconductor industry market [41]. Comparing the current leading optoelectronic material GaN, ZnO has a similar direct band gap of 3.37eV, and it has larger exciton binding energy of 60 meV, which makes it the best candidate in the area of UV LD [42]. Besides, ZnO can be synthesized at lower temperature and low cost using various methods. Its ease of etching can lower the effort and cost of device processing.

As mentioned above, the major obstacle for ZnO based optoelectronic devices is the difficulty of p-type dopping. A lot of effort has been made to achieve p-type ZnO in order to demonstrate ZnO based homojunction devices in our group. We have achieved Sb doped ZnO thin film in our MBE system [16, 43]. Ohmic contacts for both n-type and p-type ZnO have been developed [44,45]. Based on these, ZnO homojunction photodetector, LED and random lasers were fabricated and studied [46-50]. These important results are critical for further developing high efficiency LED and LD devices.

A very promising feature of ZnO is that its one dimensional nanostructure can be synthesized by various low-cost methods. These nanostructures can be excellent material for field emission devices, sensor and lasers [51-53]. In our group, we have successfully developed Sb doped and Ag doped nanowires [53, 54], and homojunction photodetector [55] and Fabry-Perot (F-P) type laser [53] have been demonstrated. But random laser device, which is another important application of nanowires, still needs to be studied.

1.3 Chapter arrangement

In this dissertation, nonvolatile memory and random laser using doped ZnO are studied. Chapter 2-4 focus on ZnO based nonvolatile memory devices including p-n-p and n-p-n memories and resistive switching memory. Chapter 5-6 focus on random lasers based on ZnO nanowires/thin film homojunctions.

In chapter 2, A ZnO p-n-p structure using Sb doped ZnO as p-type layer and undoped ZnO as n-type layer on c-plane sapphire substrate was demonstrated. First the p-type conductivity of the Sb doped ZnO thin film has been studied. Secondary ion mass

spectrometry (SIMS) result showed good interface between Sb doped and undoped layers. The formation of p-n junction was proved by the good rectification behavior between p-type layer and n-type layer by I-V measurements. A hole concentration $N_A = 5.95 \times 10^{16}\ cm^{-3}$ was obtained from the fitting of the C-V curve by using small signal model. The program and retention characteristics of the p-n-p nonvolatile memory structure related to the charge storage in the n-layer were also studied.

In chapter 3, ZnO n-p-n nonvolatile memory structure based on nanorods was achieved. First, vertically aligned Na doped nanorods were grown on a ZnO seed layer on Si. The p-type conductivity of the Na doped nanorods was studied by using low temperature photoluminescence (PL) and nanorod field effect transistor measurements. Second, vertically aligned ZnO nanotips, nanotubes and nanorods were synthesized without catalytic assistance on the p-type Na-doped ZnO nanorods. The growth mechanism was studied. The n-p-n memory structure based on the homojunction nanorod and undoped seed layer was fabricated. The programming and retention characteristics show good memory effect.

In chapter 4, current self-complianced and self-rectifying bipolar resistive switching was observed in Ag-contacted, Na-doped ZnO nanowire resistive memory. Scanning electron microscopy (SEM), high spatial resolution Auger electron spectroscopy (HSR-AES) and I-V characteristics were used to studied the resistive switching mechansim. The mechansim of self-complianced and self-rectifying bipolar resistive switching effect was discussed.

In chapter 5, a homojunction random laser device based on nitrogen doped p-type nanowires and undoped n-type thin film has been studied. P-type nitrogen doped ZnO nanowires were grown by using CVD without any metal catalyst on ZnO seed layer on silicon substrate. The p-type behavior was studied by the output characteristic and transfer characteristic of the nanowire back-gated FET and PL. The acceptor activation energy was calculated from PL and carrier concentration statistics. The lasing behaviors were studied by using both optical pumping and electrical pumping. The angle dependant EL result shows that the emission has a broad angle distribution, further indicating the formation of ZnO nanowires p-n homojunction random laser.

In chapter 6, the DBR structure was utilized to improve the performance of the random laser devices. The nitrogen doped p-type ZnO nanowires were grown on undoped n-type ZnO thin film on a 10-period DBR structure of alternative layers made from SiO_2 and SiN_x. The nanowires were studied by SEM, low temperature PL and X-ray photoelectron spectroscopy (XPS). The p-n junction was studied using the I-V characteristics and photocurrent measurements. The device was pumped electrically and the electroluminescence (EL) was studied.

Finally, a conclusion of this dissertation is presented in chapter 7.

References

[1] Ü. Özgür,Ya. I. Alivov, C. Liu, A. Teke, M. A. Reshchikov, S. Doğan, V. Avrutin, S.-J. Cho, and H. Morkoçd, J.Appl. Phys. **98**, 041301 (2005).

[2] Y. Wang, J.A. Cooper, Jr., M.R. Melloch, S.T. Sheppard, J.W. Palmour, and L.A. Lipkin, J. Electron. Mater. **25**, 5(1996).

[3] E. O. Kane, Phys. Rev. B **18**, 6849 (1978).

[4] V. A. Coleman, and C. Jagadish, Chapter 1 of Zinc Oxide Bulk, Thin Films and Nanostructures: Processing, Properties and Applications, Publisher: Elsevier Science (2006).

[5] M. Fujita, N. Kawamoto, M. Sasajima, and Y. Horikoshi, J. Vac. Sci. Technol. B **22**, 1484 (2004).

[6] M. Wei, R. C. Boutwell, N. Faleev, A. Osinsky, and W. V. Schoenfeld, J. Vac. Sci. Technol. B **31**, 041206 (2013).

[7] Z. Fan and J. G. Lu, J Nanosci Nanotechnol. **5(10)**,1561-73 (2005).

[8] D. C. Look, J. W. Hemsky, and J. R. Rizelove, Phys. Rev. Lett. **82**, 2552(1999).

[9] S. B. Zhang, S. H. Wei, and A. Zunger, Phys. Rev. B **63**, 075205(2001).

[10] Y. J. Li, T. C. Kaspar, T. C. Droubay, Z. Zhu, V. Shutthanandan, P. Nachimuthu, and S. A. Chambers, Appl. Phys. Lett. **92**, 152105 (2008).

[11] C. H. Park, S. B. Zhang, and S. H. Wei, Phys. Rev. B **66**, 073202(2002).

[12] S.S. Lin, J.G. Lu, Z.Z. Ye, H.P. He, X.Q. Gu, L.X. Chen, J.Y. Huang, and B.H. Zhao, Solid State Commun. **148**, 25-28(2008).

[13] W. Liu, F. Xiu, K. Sun, Y.H. Xie, K. L. Wang, Y. Wang, J. Zou, Z. Yang, and J. Liu, J. Am. Chem. Soc. **132**, 2498 (2010).

[14] H. He, S. Lin, G. Yuan, L. Zhang, W. Zhang, L. Luo, Y. Cao, Z. Ye, and S. T. Lee, J. Phys. Chem. C **115 (39)**, pp 19018-19022 (2011).

[15] S. Limpijumnong, S. B. Zhang, S. H. Wei, and C. H. Park, Phys. Rev. Lett. **92**, 155504 (2004).

[16] F. X. Xiu, Z. Yang, L. J. Mandalapu, D. T. Zhao, and J. L. Liu, Appl. Phys. Lett. **87**, 152101 (2005).

[17] T. Aoki, Y. Hatanaka, and D. C. Look, Appl. Phys. Lett., **76**, 3257 (2000).

[18] A. B. Yankovich, B. Puchala, F. Wang, J. -H. Seo, D. Morgan, X. Wang, Z. Ma, A. V. Kvit, and P. M. Voyles, Nano Lett. **12**, 1311-1316 (2012).

[19] L. J. Mandalapu, F. X. Xiu, Z. Yang, D. T. Zhao, and J. L. Liu, Appl. Phys. Lett. **88**, 112108(2006)

[20] J. Kong, S. Chu, M. Olmedo, L. Li, Z. Yang, and J. L. Liu, Appl. Phys. Lett. **93**, 132113(2008)

[21] S. Chu, G. Wang, W. Zhou, Y. Lin, L. Chernyak, J. Zhao, J. Kong, L. Li, J. Ren, and J. L. Liu, Nat. Nanotechnol. **6**, 506(2011)

[22] A. Tsukazaki, A. Ohtomo, T. Onuma, M. Ohtani, T. Makino, M. Sumiya, K. Ohtani, S. F. Chichibu, S. Fuke, Y. Segawa, H. Ohno, H. Koinuma, M. Kawasaki, Nature Mater. **4**, 42-46 (2005).

[23] D. C. Look, D. C. Reynolds, C. W. Litton, R. L. Jones, D. B. Eason, G. Cantwell, Appl. Phys. Lett. **81**, 1830-1832 (2002).

[24] C.C. Lin, S. Y. Chen, S. Y. Cheng, H. Y. Lee, Appl. Phys. Lett. **84**, 5040 (2004).

[25] C. H. Park, S. B. Zhang, and S. -H. Wei, Phys. Rev. B **66**, 073202 (2002).

[26] J. Li, S.-H. Wei, S.-S Li, and J.-B. Xia, Phys. Rev. B **74**, 081201(R) (2006).

[27] J. L. Lyons, A. Janotti, C. G. Van de Walle, Appl. Phys. Lett. **95**, 252105 (2009).

[28] L. Liu, J. Xu, D. Wang, M. Jiang, S. Wang, B. Li, Z. Zhang, D. Zhao, C. -X. Shan, B. Yao, and D. Z. Shen, Phys. Rev. Lett. **108**, 215501 (2012).

[29] N. Nagel, R. Bruchhaus, K. Hornik, U. Egger, H. Zhuang, H.-O. Joachim, T. Rohr, G. Beitel, T. Ozaki, and I. Kunishima, Proc. Int. Symp. VLSI Technology, p. 146.

[30] S. Tehrani, IEDM Tech. Dig. p585 (2006).

[31] N. Matsuzaki, K. Kurotsuchi, Y. Matsui, O. Tonomura, N. Yamamoto, Y. Fujisaki, N. Kitai, R. Takemura, K. Osada, S. Hanzawa, H. Moriya, T. Iwasaki, T. Kawahara, N. Takaura, M. Terao, M. Matsuoka, and M. Moniwa: IEDM Tech. Dig., p. 738 (2005).

[32] C. T. Gardner, J. A. Cooper, Jr., M. FL Melloch, J. W. Palmour, and C. H. Carter, Jr., Appl. Phys. Lett. **61**, 1185 (1992).

[33] W. Xie, J. A. Cooper, Jr., M. R. Melloch, J. W. Palmour, and C. H. Carter, Jr., IEEE Electron Dev. Lett. **15**, p212(1994).

[34] Y. Wang, J.A. Cooper, Jr., M.R. Melloch, S.T. Sheppard, J.W. Palmour, and L.A. Lipkin, J. Electron Microsc. **25**, 5(1996).

[35] A. Sawa, Mater. Today **6**, 28(2008).

[36] W.-Y. Chang, Y. -C. Lai, T. -B. Wu, S. -F. Wang, F. Chen, and M. -J. Tsai, Appl. Phys. Lett. **92**, 022110 (2008).

[37] N. Xu, L. F. Liu, X. Sun, C. Chen, Y. Wang, D. D. Han, X. Y. Liu, R. Q. Han, J. F. Kang, and B. Yu, Semicond. Sci. Technol. **23**, 075019 (2008).

[38] Y. C. Yang, F. Pan, Q. Liu, M. Liu, and F. Zeng, Nano Lett. **9 (4)**, pp1636-1643 (2009).

[39] Y. C. Yang, F. Pan, and F. Zeng, New J. Phys. **12,** 023008 (2010).

[40] J. Qi, J. Huang, D. Paulc, J. Ren, S. Chu, and J. Liu, Nanoscale **5**, 2651-2654 (2013).

[41] 2010 Optoelectronics Market Report. Databeans, Inc.

[42] Y. Chen, D. M. Bagnall, H. -J. Koh, K. -T. Park, K. Hiraga, Z. Zhu, and T. Yao, J. Appl. Phys. **84**, 3912 (1998).

[43] F. X. Xiu, Z. Yang, L. J. Mandalapu, D. T. Zhao, and J. L. Liu, Appl. Phys. Lett. **87**, 252102 (2005).

[44] L. J. Mandalapu, Z. Yang, and J. L. Liu, Appl. Phys. Lett. **90**, 252103 (2007).

[45] L. J. Mandalapu, F. X. Xiu, Z. Yang, and J. L. Liu, Solid-state Electronics **51**, 1014 (2007).

[46] L. J. Mandalapu, Z. Yang, F. X. Xiu, D. T. Zhao, and J. L. Liu, Appl. Phys. Lett. **88**, 092103 (2006).

[47] J. Kong, S. Chu, M. Olmedo, L. Li, Z. Yang, and J. Liu, Appl. Phys. Lett. **93**, 132113 (2008).

[48] S. Chu, J. H. Lim, L. J. Mandalapu, Z. Yang, L. Li, and J. L. Liu, Appl. Phys. Lett. **92**, 152103 (2008).

[49] S. Chu, M. Olmedo, Z. Yang, J. Kong, and J. Liu, Appl. Phys. Lett. **93**, 181106 (2008).

[50] J. Kong, S. Chu, Z. Zuo, J. Ren, M. Olmedo, and J. Liu, Applied Physics A **107**, 971 (2012).

[51] R. P. Sugavaneshwar, T. Nagao, and K. K. Nanda, RSC Adv. **2**, 2713-2716 (2012).

[52] T. -J. Hsueh, S. -J. Chang, C. -L. Hsu, Y. -R. Lin, and I.-C. Chen, J. Electrochem. Soc. **155**, K152-K155 (2008).

[53] S. Chu, G. Wang, W. Zhou, Y. Lin, L. Chernyak, J. Zhao, J. Kong, L. Li, J. Ren, and J. Liu, Nat. Nanotechnol. **6**, 506 (2011).

[54] G. Wang, S. Chu, N. Zhan, H. Zhou, and J. Liu, Appl. Phys. A **103**, 951 (2011).

[55] G. Wang, S. Chu, N. Zhan, Y. Lin, L. Chernyak, and J. Liu, Appl. Phys. Lett. **98**, 041107 (2011).

Chapter 2

P-n-p nonvolatile memory structure based on Sb doped and undoped ZnO thin film

2.1 Introduction

ZnO, as a II-VI wide band gap material, has attracted significant attention in the last few years [1-3]. However, due to the "intrinsic" donors such as zinc interstitials and oxygen vacancies [4, 5] and the unintentional donor hydrogen [6], reliable p-type conductivity is difficult to achieve, which poses the largest obstacle on the application of ZnO. The group V elements are considered to be p-type dopants for ZnO and a great deal of efforts have been made to achieve the p-type conductivity [7-9]. Based on first-principle calculations, antimony (Sb) can produce shallow acceptor levels in ZnO if Sb atom substitutes Zn atom and connects with two Zn vacancies [10]. Experimentally, our group achieved Sb doped p-type ZnO thin films and nanowires [11, 12] and also developed various devices based on Sb doped p-type ZnO such as photodetectors [3, 12], light emitting diodes [13] and nanowire lasing devices [14].

While all the p-type ZnO studies at the device level are based on optoelectronic devices and the applications of p-type ZnO are limited within optoelectronic field, the potential of this wide band gap material for nanoelectronic devices such as nonvolatile memory has been largely ignored. On the other hand, demonstration of ZnO nanoelectronic devices based on p-type ZnO materials will also unambiguously prove the

p-type conductivities of the materials as their optoelectronic devices had achieved [12-14]. Previously, a memory structure based on wide band gap material was fabricated and characterized using a SiC n-p-n structure [15]. This memory structure can achieve low programming voltage (≤10V) due to the diode operation mechanism and long retention time (>100 years) due to the low thermal generation current. Compared with SiC, ZnO having a band gap of ~3.2 eV can achieve extremely low thermal generation current, which can further enhance the retention performance of the nonvolatile memory [15]. ZnO is a direct band gap material which has low minority carrier lifetime (nanosecond) [16] and it will result in high programming speed. Furthermore, ZnO can also be synthesized with lower cost using low-temperature epitaxial growth so it can reduce the cost for future memory devices. In this chapter, we report the p-type Sb doped ZnO films based on Sb-ZnO/ZnO/Sb-ZnO p-n-p memory structure. The program and retention performances of this memory structure are also presented.

2.2 Material growth and device fabrication

ZnO p-n-p structure was grown using plasma-assisted molecular-beam epitaxy. First, a thin MgO buffer layer was grown on c-sapphire substrate at 450 °C for 70 s, which was followed by the growth of a ZnO buffer layer at the same substrate temperature for 15 min. Then, an Sb doped p-type ZnO / undoped n-type ZnO homojunction was grown on this MgO/ZnO buffer. The 300 nm thick undoped ZnO film was grown at a substrate temperature of 500 °C with Zn effusion cell temperature of 360 °C. This was followed by the growth of the 300 nm thick Sb doped ZnO layer at a higher

substrate temperature of 550 °C with Zn and Sb effusion cells temperature of 360 °C and 390 °C, respectively. In order to activate the Sb dopants, in situ thermal annealing was performed in vacuum at 800 °C for 20 min. To form the p-n-p memory device, photolithography and wet etching were used to define the mesa structure. Au/Ni (100/10 nm) were then deposited on p-type ZnO. Lift-off process and proper annealing were used to form Ohmic contact electrodes and SiO_2 was deposited to passivate the device. Au/Ti (100/10nm) electrodes were also fabricated on n-type ZnO for one sample, to verify the formation of the p-n junctions.

2.3 Results and discussion

Figure 2.1 shows elemental distribution of Zn, O, Sb, and Al in the sample measured by secondary ion mass spectrometry (SIMS). The Al signal is from the sapphire substrate. The sharp stair of Sb distribution between doped and undoped ZnO represents a good interface of the doped and undoped layers. The atomic percentage of Sb is estimated to be around 1.5%.

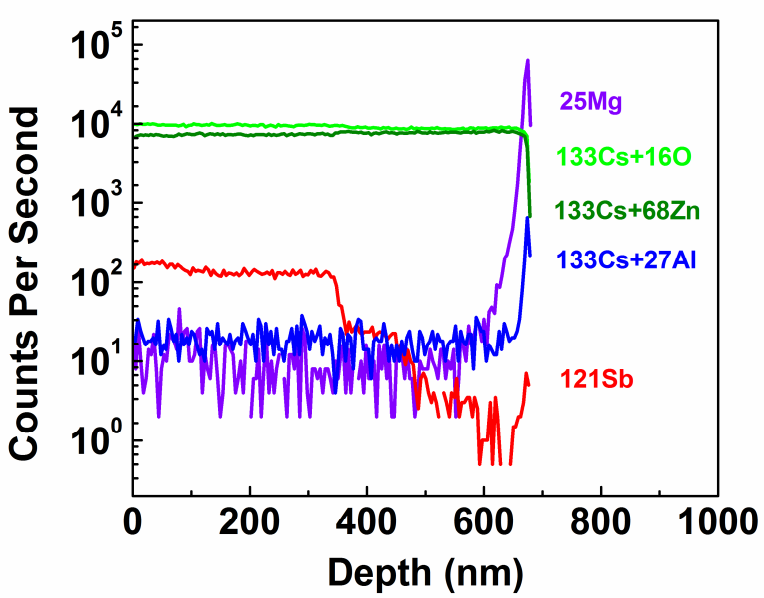

Figure 2.1. SIMS result of ZnO p-n junction on c-sapphire substrate. The elemental profiles of Zn, O, Sb, and Al can be seen, which confirms our device structure has been formed.

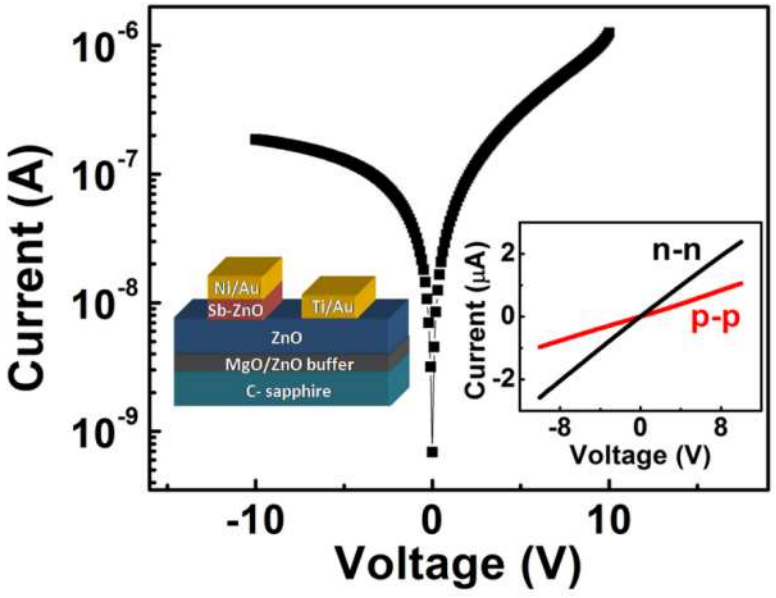

Figure 2.2. I-V characteristics of Sb-doped p-type ZnO / undoped n-type ZnO homojunction. Left inset shows the measured device structure. Right inset shows the I-V curves of p-p contacts and n-n contacts, respectively. Ohmic contact behavior is evident.

Current-voltage (I-V) characteristics were characterized by an Agilent B1500A semiconductor parameter analyzer. Figure 2.2 shows I-V characteristics of a typical p-n junction after Au/Ni to p-type ZnO and Au/Ti to n-type ZnO contacts were formed (left inset), suggesting typical diode rectifying characteristics. The right inset shows that the Ohmic contacts were formed on both p-type ZnO and n-type ZnO. These results suggest the formation of ZnO p-n junction diodes and thereby p-n-p memory structure.

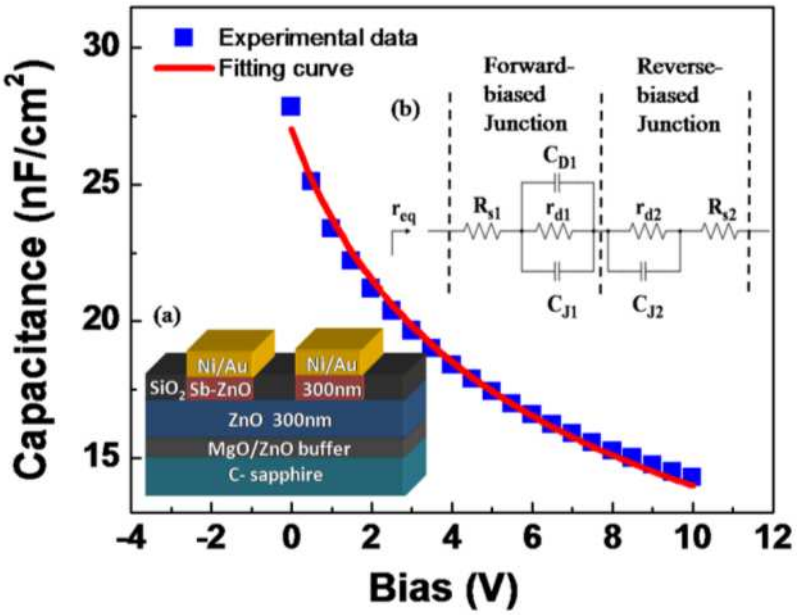

Figure 2.3. C-V characteristics of ZnO p-n-p structure on sapphire. The symbols are the experimental data and the solid line is the fitting result based on small signal model. Inset (a) shows the measured p-n-p memory structure. Inset (b) shows the equivalent circuit of the p-n-p structure.

From Hall effect measurement, the electron concentration, mobility and resistivity of the undoped ZnO layer are $3.46 \times 10^{17}\ cm^{-3}$, 17.6 $cm^2V^{-1}s^{-1}$ and 1.03 Ωcm, respectively. However, it is impossible to extract accurate hole carrier concentration of the top Sb-ZnO thin film of the structure by using Hall effect measurement due to the thick underneath undoped n-type layer. In order to study the p-type behavior of the Sb-ZnO thin film, capacitance-voltage (C-V) characteristics were obtained using a 4284A LCR meter. Figure 2.3 shows high-frequency (1 MHz) C-V characteristic of the ZnO p-n-p structure (inset (a) in Figure 2.3). The capacitance was measured between the two Au/Ni contacts. The C-V sweep ranges from 0V to 10V. As seen from the figure, the capacitance of the device decreases nonlinearly as the applied bias increases.

To quantitatively understand the C-V characteristics and extract hole concentration in the Sb-doped p-type ZnO layer, we can use the small signal model. An equivalent circuit of the p-n-p structure is shown as an inset (b) in Figure 2.3. The impedance r_{eq} of this symmetric p-n-p structure can be calculated:

$$\begin{aligned} r_{eq} &= R_{s1} + r_{d1} \parallel \frac{1}{j\omega C_{D1}} \parallel \frac{1}{j\omega C_{J1}} + r_{d2} \parallel \frac{1}{j\omega C_{J2}} + R_{s2} \\ &= R_{s1} + \frac{r_{d1}}{j\omega r_{d1}(C_{D1} + C_{J1}) + 1} + \frac{r_{d2}}{j\omega r_{d2} C_{J2} + 1} + R_{s2} \\ &= R_{s1} + R_{s2} + \frac{1}{\omega^2 r_{d1}(C_{D1} + C_{J1})^2} + \frac{1}{j\omega \dfrac{(C_{D1} + C_{J1})C_{J2}}{C_{D1} + C_{J1} + C_{J2}}}, \end{aligned} \qquad (1)$$

where the imaginary part $j\omega\frac{(C_{D1}+C_{J1})C_{J2}}{C_{D1}+C_{J1}+C_{J2}}$ clearly shows that the total capacitance can be viewed as $C_{D1}+C_{J1}$ in series with C_{J2}.The reverse-biased junction capacitance C_{J2} can be calculated by:

$$C_{J2}=\frac{\varepsilon A}{x_n+x_p}=\frac{\varepsilon A}{\sqrt{\frac{2\varepsilon(V_{bi}+V_A)}{q(N_A+N_D)}(\sqrt{\frac{N_A}{N_D}}+\sqrt{\frac{N_D}{N_A}})}}. \qquad (2)$$

Here, ε is dielectric constant, A is area, q is electron charge, V_{bi} is the built-in potential of the p-n junction, x_n and x_p are the depletion region thicknesses in n-type and p-type ZnO, respectively, and N_A and N_D are acceptor and donor concentration, respectively. Because the reverse-biased junction and forward-biased junction are in series, the voltage drop across the forward-biased junction only shares a very small portion of the applied bias. Thus, the diffusion capacitance C_{D1} can be ignored and the junction capacitance of a forward-biased junction is calculated by

$$C_{J1}=A\sqrt{\frac{8\varepsilon qN_AN_D}{V_{bi}(N_A+N_D)}}.$$

So for the p-n-p structure, the total capacitance is:

$$C(V_g)=\frac{C_{J1}\times C_{J2}(V_g)}{C_{J1}+C_{J2}(V_g)}. \qquad (3)$$

From the fitting by using the equation (3) (the solid line in Figure 2.3) and the electron concentration of $3.46\times10^{17}\,cm^{-3}$, $N_A=5.95\times10^{16}\,cm^{-3}$ and $V_{bi}=2.71\,V$ have been obtained.

The decrease of the capacitance at higher voltage also suggests that this p-n-p structure can act as a charge storage device. When a bias is applied on the p-n-p structure, one p-n junction is forward-biased while the other one is reverse-biased. The electrons

inside the n-layer flow out of the structure from the forward-biased junction, while the n-layer also receives small amount of electrons from the reverse-biased junction until the potential of the n-layer cannot increase further under this applied voltage. The net effect is the built-up of positive space charges inside the n-type layer, or charging the n-layer. In the mean time, the width of the space charge region of the reverse-biased p-n junction increases.

To evaluate the charging, or programming operation, an Agilent 81104A pulse generator was used to operate the device and the capacitance was read from an Agilent 4284A LCR meter at 0V. In this situation, after the bias is removed, the programmed extra space charges in the n-layer will redistribute and reverse both p-n junctions. The space charge region width of both junctions is larger and thus the capacitance is smaller than that of the junctions before programming. Figure 2.4(a) shows capacitance change (ΔC) as a function of different program pulse height. The pulse width was fixed at 1 s. Under the program pulse larger than 2 V, the absolute value of ΔC increases as the pulse height increases, which indicates that more charges are developed inside the structure under higher pulse. Figure 2.4(b) shows ΔC for different pulse width. The pulse height was fixed at 10V and the pulse width was changed from 1 μs to 1 s. The absolute value of ΔC begins to increase after the pulse width is larger than 10 μs and reaches saturation at 0.1 s. This programming speed is slow but reasonable considering the low voltage operation.

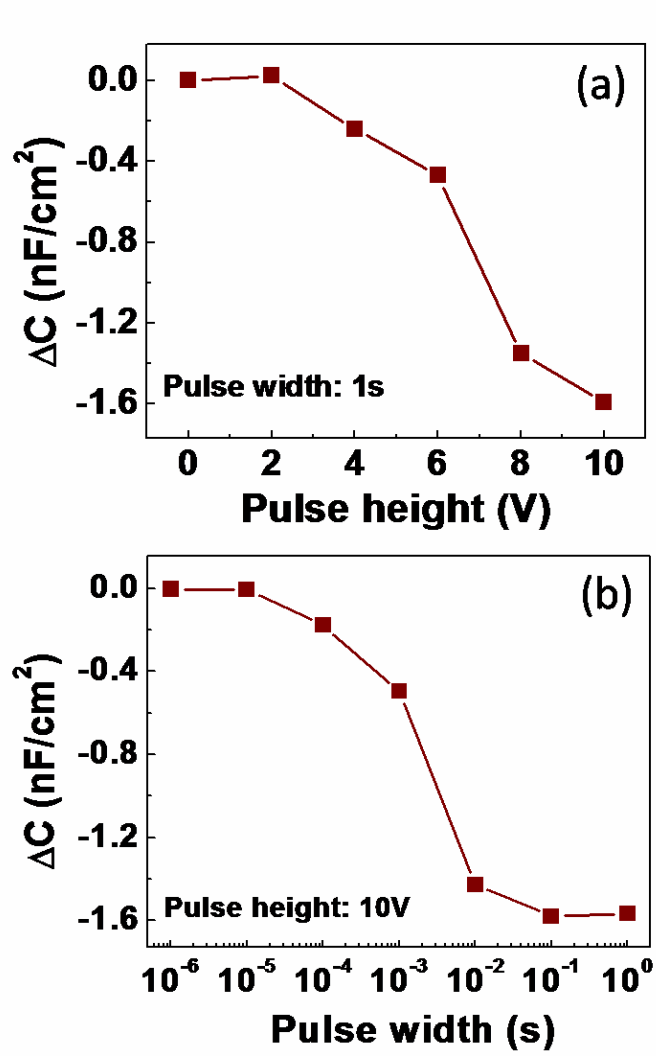

Figure 2.4. Programming performance of ZnO p-n-p memory structure. ΔC is the change of the capacitance before and after programming. All the capacitance is read at 0V bias. (a) Using programming pulses with different pulse height and 1 s pulse width. (b) Using programming pulses with different pulse width and 10V pulse height.

Figure 2.5 shows retention characteristics of the ZnO p-n-p structure. The device was programmed with 10V for 1 ms, and the capacitance measured at 0V was plotted as a function of the waiting time. After the programming, excess space charges are developed and reverse-bias both p-n junctions. The reverse-biased p-n junctions have net generation rate and the carriers from thermal generation will neutralize the excess space charges until both junctions return to equilibrium. As the thermal generation rate is exponential to the reciprocal of the band gap energy, it will take extremely long time for a defect free device to return to thermal equilibrium. However, the defects are unavoidable in the ZnO, and these defects will help the generation process and thus neutralize some excess space charges. As seen from the figure, during the early stage, the capacitance increases about 20% of the total ΔC after programming. This shall be due to the thermal generation of both bulk Shockley-Read-Hall defect levels and other levels originated from surface states. After 10^4 s, the capacitance remains almost constant, which indicates the amount of the charges trapped inside the structure become stable. This result suggests that the defects in the present material do not significantly discharge the device and this ZnO p-n-p structure is capable of achieving much longer retention time than the flash memory, which usually meets 10-year retention standard.

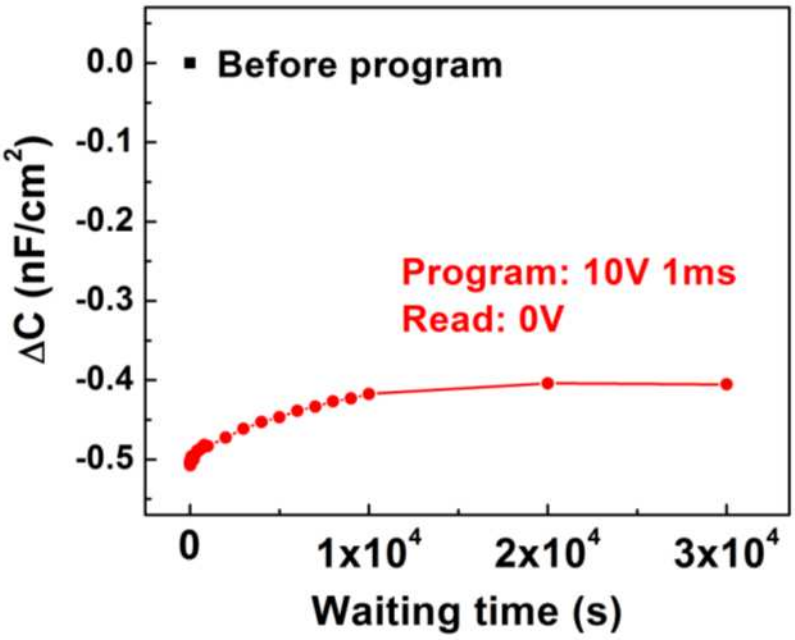

Figure 2.5. Retention characteristics of ZnO p-n-p memory structure. A pulse of 10V for 1ms was used to program the device before the retention measurement.

2.4 Summary

In summary, a ZnO p-n-p structure using Sb doped ZnO as p-type layer and undoped ZnO as n-type layer on c-plane sapphire substrate was fabricated. SIMS result showed good interface between Sb doped and undoped layers. The formation of p-n junction was proved by the good rectification behavior between p-type layer and n-type layer by I-V measurements. A hole concentration $N_A = 5.95 \times 10^{16}\ cm^{-3}$ was obtained from the fitting of the C-V curve by using small signal model, which cannot be done by Hall effect measurement due to the underneath n-type layer. The nonvolatile memory effect of the p-n-p structure related to the charge storage in the n-layer of the p-n-p

structure was also studied. The program and retention characteristics showed that ZnO p-n-p memory structure can achieve low operation voltage and long retention time, which suggests that the Sb doped p-type ZnO could be excellent material for future nonvolatile memory application.

References

[1] Ü. Özgür, Ya. I. Alivov, C. Liu, A. Teke, M. A. Reshchikov, S. Doğan, V. Avrutin, S.-J. Cho, and H. Morkoç, J. Appl. Phys. **98**, 041301(2005)

[2] J.-H. Lim, C.-K. Kang, K.-K. Kim, I.-K. Park, D.-K. Hwang, and S.-J. Park, Adv. Mater. **18**, 2720(2006)

[3] G. Wang, S. Chu, N. Zhan, Y. Lin, L. Chernyak, and J. Liu, Appl. Phys. Lett. **98**, 041107(2011)

[4] D. C. Look, J. W. Hemsky, and J. R. Rizelove, Phys. Rev. Lett. **82**, 2552(1999)

[5] S. B. Zhang, S. H. Wei, and A. Zunger, Phys. Rev. B **63**, 075205(2001)

[6] Y. J. Li, T. C. Kaspar, T. C. Droubay, Z. Zhu, V. Shutthanandan, P. Nachimuthu, and S. A. Chambers, Appl. Phys. Lett. **92**, 152105(2008)

[7] A. Tsukazaki, A. Ohtomo, T. Onuma, M. Ohtani, T. Makino, M. Sumiya, K. Ohtani, S. F. Chichibu, S. Fuke, Y. Segawa, H. Ohno, Hi. Koinuma, and M. Kawasaki, Nat. Mater. **4**, 42(2005)

[8] K. K. Kim, H. S. Kim, D. K. Hwang, J. H. Lim, and S. J. Park, Appl. Phys. Lett. **83**, 63(2003)

[9] J.C. Fan, Z. Xie, Q. Wan, and Y.G. Wang, J. Cryst. Growth **307**, 66(2007)

[10] S. Limpijumnong, S. B. Zhang, S. H. Wei, and C. H. Park, Phys. Rev. Lett. **92**, 155504(2004)

[11] F. X. Xiu, Z. Yang, L. J. Mandalapu, D. T. Zhao, and J. L. Liu, Appl. Phys. Lett. **87**, 252102 (2005)

[12] L. J. Mandalapu, F. X. Xiu, Z. Yang, D. T. Zhao, and J. L. Liu, Appl. Phys. Lett. **88**, 112108(2006)

[13] J. Kong, S. Chu, M. Olmedo, L. Li, Z. Yang, and J. L. Liu, Appl. Phys. Lett. **93**, 132113(2008)

[14] S. Chu, G. Wang, W. Zhou, Y. Lin, L. Chernyak, J. Zhao, J. Kong, L. Li, J. Ren, and J. L. Liu, Nat. Nanotechnol. **6**, 506(2011)

[15] Y. Wang, J.A. Cooper, Jr., M.R. Melloch, S.T. Sheppard, J.W. Palmour, and L.A. Lipkin, J. Electron. Mater. **25**, 5(1996)

[16] K. Moazzami, T.E. Murphy, J.D. Phillips, M.C.-K. Cheung, and A.N. Cartwright, Semicond. Sci. Technol. **21**, 717(2006)

Chapter 3

N-p-n nonvolatile memory based on ZnO vertically aligned homojunction nanostructures and undoped thin film

3.1 Introduction

ZnO attracted significant attention in the last few years due to its wide band gap of 3.37 eV, large exciton binding energy of 60 meV, and easy formation of diverse nanoscale morphology [1-4]. These various nanostructures, which can be synthesized by different methods such as solution synthesis [5], chemical vapor deposition (CVD) [6] and physical vapor deposition (PVD) [7], have been used for various applications. For examples, ZnO nanotip can be an excellent structure for field emission devices [1]; ZnO tubular structure can be used as sensor due to its large surface [8]; one-dimensional nanowires can serve as excellent optical medium for lasers [6, 9]. Although these different nanostructures such as nanotips, nanotubes and nanorods have been demonstrated separately by different methods, the controllable growth of these nanostructures, especially highly orientated ones, using the same technique will definitely benefit the applications of these nanostructures and has not been reported yet. In this research, we achieved different vertically aligned one-dimensional ZnO nanostructures using CVD on top of vertically aligned Na-doped nanorods. The Na-doped nanorods were grown on a ZnO seed layer and exhibit p-type conductivity from the nanorod back-gated field effect transistor (FET) measurements. An n-p-n memory structure formed by

the undoped seed layer and nanorod homojunction exhibited reasonable programming and retention characteristics.

3.2 Nanostructures growth

Na-doped ZnO nanorods were grown in a quartz tube furnace system under atmospheric pressure. Zinc powder in a silica bottle was placed in the center of the quartz tube. A Si (100) substrate with a ZnO seed layer on top was kept 2 cm away from the Zn source at the downstream side. The undoped ZnO seed thin film was grown by molecular beam epitaxy. The film consists of closely packed columnar structures due to the preferential growth of wurtzite ZnO along c-axis direction. The thickness of the film is about 1400 nm. The size of the substrate with seed layer is 1 cm in width and 2 cm in length. In addition, in order to subsequently form metal contact to the undoped film, portion of the substrate of about 0.5 cm in length was covered by a piece of silicon during the growth. $NaNO_3$ powder was placed in a silica bottle at upstream side. Nitrogen gas with a flow rate of 1000 s.c.c.m. passed continuously through the furnace as the carrier gas. The source and substrate were then heated to the growth temperature of 700 ℃. During the growth, a mixture gas of argon/oxygen (99.5%/0.5%) of 300 s.c.c.m. was introduced to the quartz tube. The growth time was 10 min.

3.2 P-type Na doped ZnO nanorods

Figure 3.1 (a) shows an SEM image of the as-grown Na-doped ZnO nanorods. The inset is a side view SEM image of the cleaved sample. Na-doped vertically aligned nanorods on the ZnO seed layer are evident. The diameters of the nanorods vary and should be related to the size nonuniformity of columnar structures in the seed layer. Figure 3.1 (b) shows the temperature-dependent photoluminescence (PL) spectra of the Na-doped ZnO nanorods. A He-Cd laser with an excitation wavelength of 325nm was used in this experiment. The peak at 3.356 eV at 15 K can be attributed to the acceptor bound exciton (*AX*) recombination [10-12]. The peaks at around 3.289 eV and 3.227 eV at 15 K blue-shift as the increase of temperature and can be assigned to free electron to acceptor (*FA*) emission and donor-acceptor-pair (*DAP*) emission, respectively [10, 13]. The longitudinal-optical (*LO*) phonon replica of the *DAP* emission at 3.157 eV is shifted by the ZnO phonon energy of ~70 meV. The activation energy of an acceptor ΔE_A can be estimated with the equation [14] $\Delta E_A = E_{gap} - E_{DAP} - \Delta E_D + < \frac{e^2}{4\pi\varepsilon_0\varepsilon_{ZnO} r_{DAP}} >$. The donor binding energy ΔE_D is about 30 meV [15, 16] and the intrinsic band gap $E_{gap} = 3.436\ eV$ at 15 K [15]. ε_{ZnO} is the dielectric constant of ZnO (8.6). r_{DAP} is the average donor-acceptor pair distance. The last term represents the Coulomb interaction between the donors and acceptors and the value is around 20 meV [14]. Thus, the acceptor activation energy ΔE_A for the Na acceptor is estimated to be around 200 meV.

To study the electrical transport properties of the nanorods, a nanorod back-gated FET was fabricated. The Na-doped ZnO nanorods were transferred onto a SiO_2 (300

nm)/p+-Si wafer and then Ni/Au electrodes were formed on a nanorod by using photolithography and e-beam evaporation. Al was deposited on the back of the Si wafer as the back gate electrode. An SEM image of an as-fabricated device is shown in the inset of Figure 3.1 (c). The I_d-V_g curve shown in Figure 3.1 (c) exhibits clear field effect characteristic of p-type conductivity: as the gate voltage increases, the drain current of the nanorod decreases. However the threshold voltage is around 0 V, therefore the hole concentration is difficult to estimate. Considering the low drain current, this result may be due to the low hole concentration of the nanorod. The low hole concentration should be the result of strong compensation from various unintentional donors such as Zn interstitials, oxygen vacancies, and hydrogen complexes [17-19]. The low threshold voltage may also be related to the unavoidable Na contamination during the transfer of Na-doped nanorods onto the SiO_2. The mobile ion contamination is a common reason of the threshold voltage drift in a MOSFET. The output characteristics (I_d-V_d) of the device as shown in Figure 3.1 (d) also confirm the p-type conductivity. The nonlinear I_d-V_d curves indicate the existence of the non-ohmic contacts between the metal and high-resistivity p-type nanorod. However, after two months, the p-type conductivity of the nanorod decreased about two orders of magnitude and the nanorod became highly resistive from the FET measurement. The stability of the p-type Na-doped ZnO nanorods in air is still an issue.

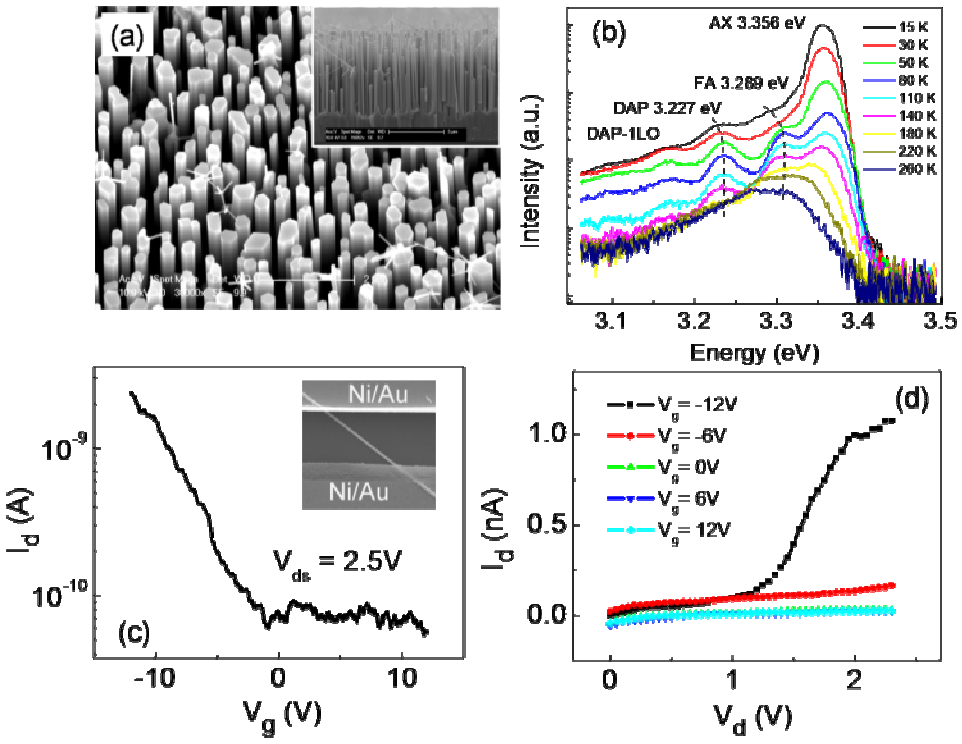

Figure 3.1. (a) SEM image of Na-doped ZnO nanorods. The inset is the sideview SEM image of the cleaved sample. (b) Temperature-dependent PL spectra of Na-doped ZnO nanorods. (c) I_d-V_g curve of Na-doped nanorod back-gated FET. Inset: SEM image of the nanorod FET device. (d) I_d-V_d curves of Na-doped ZnO nanorod back-gated FET.

3.3 Vertically aligned one-dimensional ZnO nanostructures

After the growth of Na-doped nanorods, the sample was taken out of the cooled quartz tube and then immediately transferred into another tube for subsequent growth of the undoped section. The growth configuration was the same but without Na source. Three samples with different growth time were grown. For sample A, the growth time of Na-doped nanorods and the undoped section on top was 4 min each. For sample B and C, the Na-doped nanorods were grown for 10 min while the undoped section growth

duration was 4 min and 8 min, respectively. Different growth time leads to different types of one-dimensional ZnO nanostructures on top of these Na-doped nanorods. For sample A, after the 4 min undoped ZnO growth, vertically aligned nanotips were grown mainly at the edge of top facets of the Na-doped nanorods (Figure 3.2 (a)). Different from sample A, nanotubes were formed on top of Na-doped nanorods in sample B (Figure 3.2 (b)) while nanorods were formed on top of Na-doped nanorods in sample C (Figure 3.2 (c)). To investigate the growth mechanism of the nanostructures, Figure 3.3 shows SEM images of the samples at different stages. As shown in i-iii of Figure 3.3 (a), the nucleation mainly took place at the edge of the top facets of the nanorods in sample A; as the growth time increases to 4 min, the undoped ZnO became longer to form the nanotips. However, on the 10 min Na-doped nanorods (Figure 3.3 (b)-i), 4 min growth of the undoped ZnO led to the tubular structures (Figure 3.3 (b)-ii and iii); at a longer growth time of 8 min, the tubular structures disappeared and the nanorod structures formed (Figure 3.3 (b)-iv).

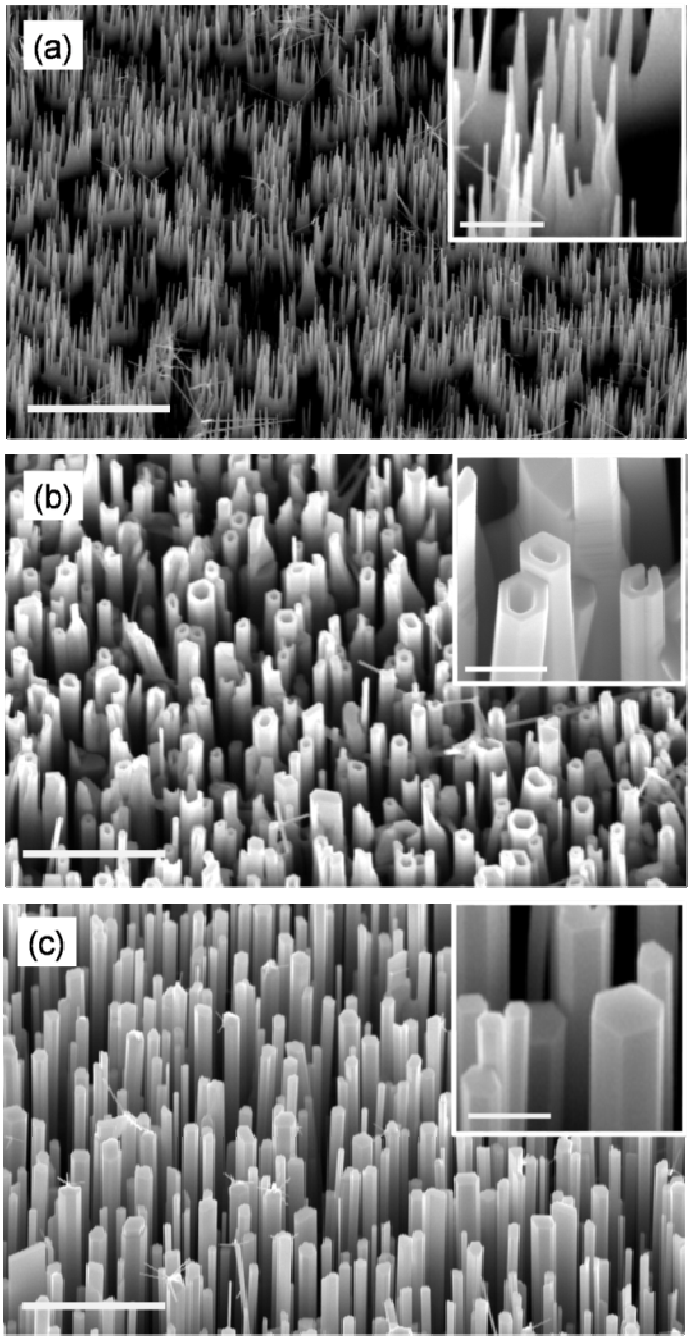

Figure 3.2. SEM images of different samples: (a) sample A, (b) sample B and (c) sample C. The scale bars are 3 μm. The inset of each image is the high-magnification SEM image. The scale bars are 500 *nm*.

Because no catalyst was used during the growth, the formation of ZnO nanostructures should follow a self-seeding vapor-solid (VS) growth mechanism. During the growth, the Zn powder was heated to form Zn vapor, which diffused out of the silica bottle and transported by the carrier gas. At a substrate temperature of 700 ℃, the desorption effect is strong and it is difficult to form ZnO seeds on the whole surface of top facets of the short Na-doped nanorods (Figure 3.3 (a)-i), especially under the high gas flow rate (1000 sccm N_2 and 300 sccm Ar/O_2 in mixture), i.e., the low Zn vapor concentration. Discrete seeds formed at the edge or at some defect points on top of the nanorods (Figure 3.3 (a)-ii). The crystals grew from the seeds and formed the nanotips (Figure 3.3 (a)-iii). In contrast, for sample B and C, the Na-doped ZnO nanorods are very dense as a result of the 10 min growth (Figure 3.1 (a) and inset); the speed of the carrier gas near the top of the nanorods was decreased. A higher Zn vapor concentration was achieved around the top of the nanorods, leading to the formation of the continuous seed layer around the edge. The ZnO walls grew from these seeds and tubular structures formed (Figure 3.3 (b)-ii). When the tubular structure became longer, although the atom desorption was still strong due to the high temperature, the semi-enclosed tubular structures could trap the atoms and thus a high Zn vapor concentration formed inside the nanotubes. The nucleation and growth took place inside the nanotubes. Because of the faster growth rate under the Zn-rich condition [20], the inside wall of the tubes grew faster and solid nanorods formed at a longer growth time (Figure 3.3 (b)-iii and iv).

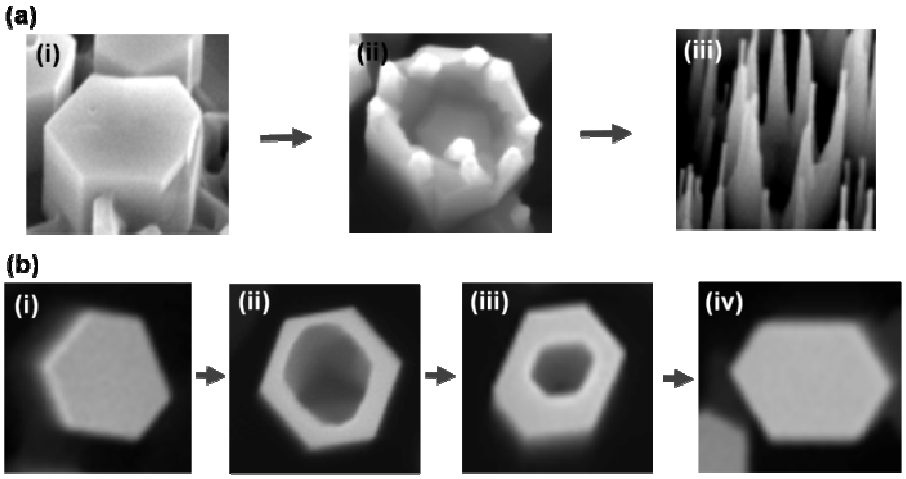

Figure 3.3. SEM images showing a gradual evolution process of the nanostructures. (a) Different stages of sample A from (i) Na-doped nanorod basement to (ii) formation of discrete ZnO seeds at the edge of the top facet, and to (iii) top undoped nanotips. (b) Different stages of sample B and C from (i) Na-doped nanorod basement, to (ii)top undoped nanotube with thin wall, to (iii) top undoped nanotube with thick wall, to (iv) top undoped nanorod.

3.4 N-p-n memory structures

The undoped nanorod/Na-doped nanorod/undoped thin film can function as an n-p-n memory structure. Earlier effort on n-p-n or p-n-p wide band gap memory structures were based on SiC [21] and ZnO thin films [22], and there is no report on nanorod structures. A demonstration of nanorod wide-bandgap semiconductor memory would represent a first step toward ultimate scaling of this type of nonvolatile memories. Here, Ti/Au (10 nm / 100 nm) was used to form Ohmic contacts on the ZnO thin film and the top end of the undoped nanorods, as shown in the inset of Figure 3.4(a). Polymethyl methacrylate (PMMA) was spun onto the sample to protect the bottom ZnO film as well as the Na-doped nanorods and support the Ti/Au top contact to the undoped ZnO nanorod section.

The top electrode is 400 μm by 400 μm. The thickness of the n-type film is about 1400 nm. The lengths of the Na-doped nanorod section and the undoped nanorod section are about 7.5 μm and 6 μm, respectively. An Agilent 81104A pulse generator was used to operate the device and the capacitance was read from an Agilent 4284A LCR meter. Figure 3.4 (a) shows the capacitance change (ΔC) read at 3 V for different programming pulse height. The voltage pulse width was fixed at 1 s and the pulse height was changed from 6V to 13V. The absolute value of ΔC begins to increase after the pulse height is larger than 6V and reaches maximum at 12 V. Figure 3.4 (b) shows the ΔC read at 3 V as a function of different programming pulse width. The pulse height was fixed at 8 V and the pulse width was changed from 10 ns to 1 s. The absolute value of ΔC begins to increase after the pulse width is larger than 10 ns and continues to increase as the pulse width becomes larger. The change of the capacitance indicates the storage of the space charge in the memory structure. When the programming pulse is applied on the n-p-n structure, one p-n junction is forward-biased while the other one is reverse-biased. The holes inside the p-type rods flow out of the structure from the forward-biased junction and build up negative space charges inside the p-type rods. After programming, the excess space charges store inside the structure and reverse-bias both p-n junctions (Figure 3.4 (b) inset) and thus the capacitance of the structure decreases. We also note that the absolute value of ΔC decreases after 12V programming pulse (Figure 3.4 (a)). This should be due to the Zener effect at high voltage. The electrons at the valence band tunnel out of the p-type region through the reverse-biased junction via the forbidden gap and thus develop compensative holes in the p-type region.

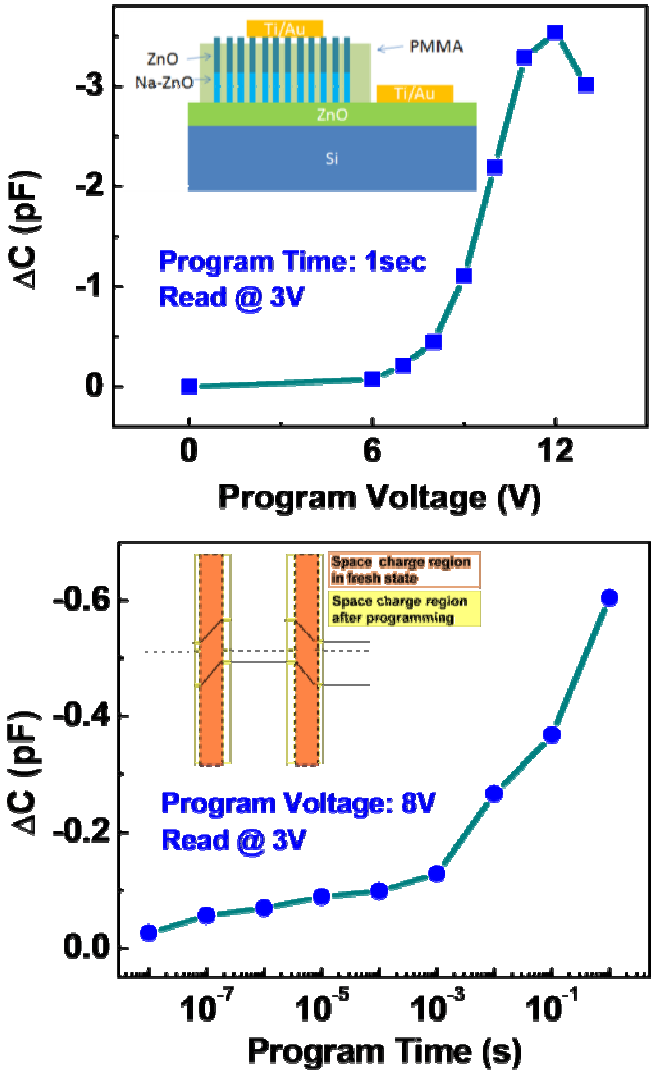

Figure 3.4. Programming characteristics of ZnO n-p-n memory device. ΔC is the change of the capacitance before and after programming. (a) ΔC as a function of programming pulses with different pulse height and 1 s pulse width. Inset: Schematic of the n-p-n memory device. (b) ΔC as a function of programming pulses with different pulse width and 8V pulse height. Inset: energy band diagram of the n-p-n structure showing the space charge region before and after programming.

After the removal of the programming voltage and at the beginning of the retention, excess space charges redistribute in the p-type section to reverse-bias both p-n junctions. Both junctions are in nonequilibrium state and have net generation rates, and thus the carriers from thermal generation will neutralize the excess space charges until both junctions return to equilibrium. This process will take extremely long time because the thermal generation rate is exponential to the reciprocal of the band gap energy [21, 22]. Figure 3.5 shows the retention characteristic of the n-p-n memory structure. The capacitance decreases after the programming and increases as the waiting time increases. The extrapolation of the data suggests that there will not be significant change of capacitance even after 10 years, which indicates a good retention.

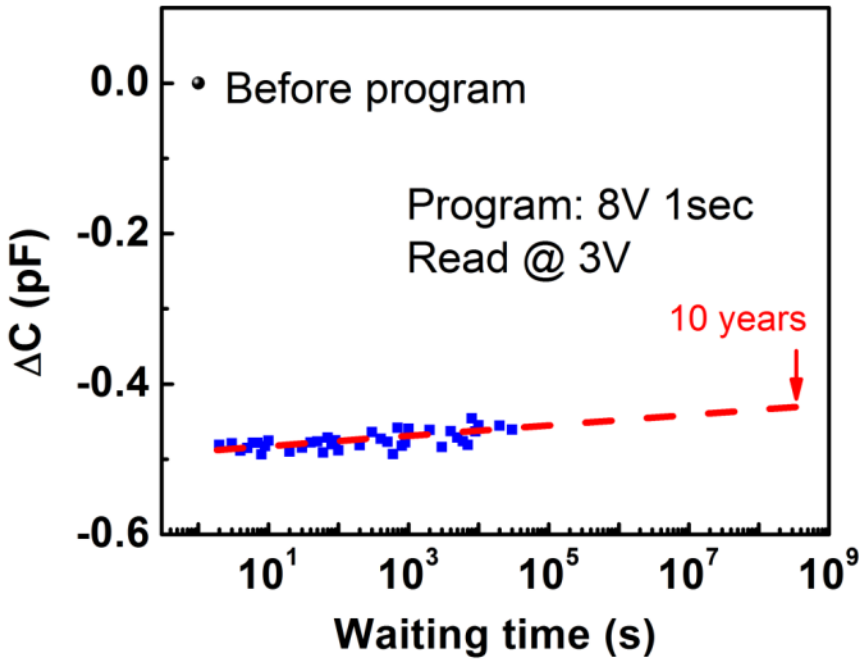

Figure 3.5. Retention characteristic of ZnO n-p-n memory structure programmed at 8V for 1s.

3.5 Summary

In conclusion, vertically aligned Na-doped nanorods were grown on a ZnO seed layer on Si via CVD at 700 ℃. The Na-doped nanorods were studied by the temperature-dependent photoluminescence and activation energy of ~200 meV was estimated. The p-type conductivity of the Na-doped nanorods was further confirmed by the output and transfer characteristics of the nanorod back-gated FET. Vertically aligned ZnO nanotips, nanotubes and nanorods were synthesized without catalytic assistance on the p-type Na-doped ZnO nanorods. The different morphology originates from different Zn vapor concentration. The n-p-n memory structure based on the homojunction nanorod and undoped seed layer was fabricated. The programming and retention characteristics show good memory effect and in turn, confirm the formation of the p-n homojunction nanorods. These diverse vertically aligned nanostructures on p-type ZnO nanorods are promising for future nanoelectronics and optoelectronic applications.

References

[1] R. P. Sugavaneshwar, T. Nagao, and K. K. Nanda, RSC Adv. **2**, 2713-2716 (2012).

[2] Y. Wei, Y. Ding, C. Li, S. Xu, J. -H. Ryo, R. Dupuis, A. K. Sood, D. L. Polla, and Z. L. Wang, J. Phys. Chem. C **112**, 18935-18937 (2008).

[3] G. -W. She, X. -H. Zhang, W. -S. Shi, X. Fan, J. C. Chang, C. -S. Lee, S. -T. Lee, and C.-H. Liu, Appl. Phys. Lett. **92**, 053111 (2008).

[4] D. -S. Yang, C. Lao, and A. H. Zewail, Science **321**, 5896 (2008).

[5] S. Xu, and Z. L. Wang, Nano Res. **4**, 1013-1098 (2011).

[6] S. Chu, G. Wang, W. Zhou, Y. Lin, L. Chernyak, J. Zhao, J. Kong, L. Li, J. Ren, and J. Liu, Nat. Nanotechnol. **6**, 506 (2011).

[7] M. Lucas, Z. L. Wang, and E. Riedo, Phys. Rev. B **81**, 045415 (2010).

[8] T. -J. Hsueh, S. -J. Chang, C. -L. Hsu, Y. -R. Lin, and I.-C. Chen, J. Electrochem. Soc. **155**, K152-K155 (2008).

[9] J. Huang, S. Chu, J. Kong, L. Zhang, C. M. Schwarz, G. Wang, L. Chernyak, Z. Chen, and J. Liu, Adv. Opt. Mater. **1**, 179-185 (2013).

[10] W. Liu, F. Xiu, K. Sun, Y. -H. Xie, K. L. Wang, Y. Wang, J. Zou, Z. Yang, and J. Liu, J. AM. Chem. Soc. **132**, 2498 (2010).

[11] W. W. Liu, B. Yao, Z. Z. Zhang, Y. F. Li, B. H. Li, C. X. Shan, J. Y. Zhang, D. Z. Shen, and X. W. Fan, J. Appl. Phys. **109**, 093518 (2011).

[12] B. Q. Cao, M. Lorenz, A. Rahm, H. von Wenckstern, C. Czekalla, J. Lenzner, G. Benndorf, and M Grundmann, Nanotechnology **18**, 455707 (2007).

[13] D. Yu, L. Hu, S. Qiao, H. Zhang, S. -E. A. Len, L. K. Len, Q. Fu, X. Chen, and K. Sun, J. Phys. D: Appl. Phys. **42**, 055110 (2009).

[14] D. C. Look, B. Claflin, Phys. Stat. Sol. B **241**, 624-630 (2004).

[15] B. K. Meyer, H. Alves, D. M. Hofmann, W. Kriegseis, D. Forster, F. Bertram, J. Christen, A. Hoffmann, M. Straßburg, M. Dworzak, U. Haboeck, and A. V. Rodina, Phys. Stat. Sol. B **241**, 231-260 (2004).

[16] V. Avrutin, D. J. Silversmith, and H. Morkoc, Proc. IEEE **98**, 1269-1280 (2010).

[17] D. C. Look, J. W. Hemsky, and J. R. Rizelove, Phys. Rev. Lett. **82**, 2552 (1999).

[18] S. B. Zhang, S. H. Wei, and A. Zunger, Phys. Rev. B **63**, 075205 (2001).

[19] Y. J. Li, T. C. Kaspar, T. C. Droubay, Z. Zhu, V. Shutthanandan, P. Nachimuthu, and S. A. Chambers, Appl. Phys. Lett. **92**, 152105 (2008).

[20] H. -J. Ko, T. Yao, Y. Chen, and S. -K. Hong, J. Appl. Phys. **92**, 4354 (2002).

[21] Y. Wang, J.A. Cooper, Jr., M.R. Melloch, S.T. Sheppard, J.W. Palmour, and L.A. Lipkin, J. Electron. Mater. **25**, 5 (1996).

[22] J. Huang, Z. L. Li, S. Chu, and J. L. Liu, Appl. Phys. Lett. **101**, 232102 (2012).

Charpter 4

Current self-complianced and self-rectifying resistive switching memory based on single Na doped ZnO nanowire

4.1. Motivation

Resistive switching memory (RSM) has been reported as a prominent candidate of next-generation nonvolatile memory because of its simple structure, high-density integration, low power consumption, fast operation and strong potential for multilevel-per-cell memories [1-4]. Recently, nanoscale RSM has also been linked to the reconfigurable logic applications [5, 6] and the concept of memristors [7-9] for analogue circuit [10] and neuromorphic computing [11-13] applications. It is generally believed that the crossbar resistive memory array will yield the most cost-effective solid-state memory. In the crossbar resistive memory array, the resistive switching materials will be placed as cross-points in between the crossbars of top metal lines and bottom metal lines (Figure 4.1). However, each memory cell at the cross point needs a diode to avoid the misreading caused by the sneak current, especially for bipolar resistive switching, in which a more complicated Zener diode simultaneously satisfying several crucial requirements is needed for each cell [14]. This situation presents extra challenges for the development of 1D1R-based bipolar resistive memory arrays, especially in 3-dimensional multi-layer stack. Furthermore, a current compliance is indispensable to prevent RSM from hard breakdown [15]. In this chapter, we report current self-rectifying and self-complianced resistive switching in single Na-doped ZnO nanowire. The current self-

rectifying can provide a solution to suppress sneak current in crossbar arrays [16], while self-compliance can prevent RSM from hard breakdown.

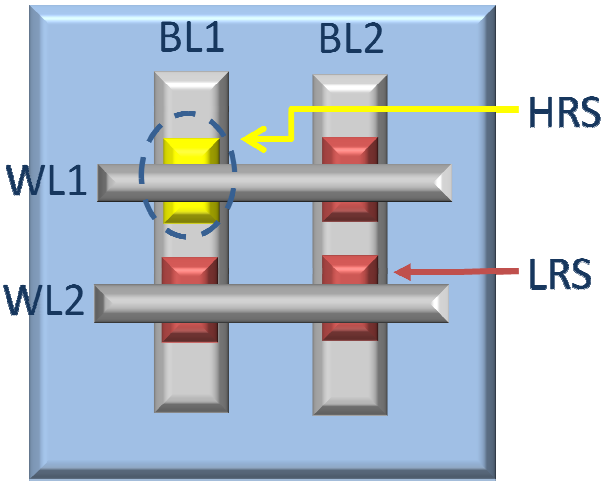

Figure 4.1. Schematic of cross bar resistive memory structure.

4.2 Experiments

Na-doped and undoped ZnO nanowires were grown in a quartz tube furnace system. Zinc powder mixed with or without sodium acetate powder in a quartz bottle was placed in the center of the quartz tube. A Si (100) substrate with 10 nm gold catalyst on top was kept 2 cm away from the source on the downstream side. Nitrogen gas with a flow rate of 1000 sccm passed continuously through the furnace. The source and substrate were then heated to growth temperature of 540 °C. During the growth, a mixture of argon/oxygen (99.5:0.5) of 300 sccm was introduced to the quartz tube for ZnO nanowire growth. The growth lasted for 30 min. The microstructure, composition and crystallinity of nanowires were evaluated by scanning electron microscopy (SEM), high resolution transmission electron microscopy (HRTEM) and secondary ion mass

spectroscopy (SIMS). The single-nanowire devices were utilized to evaluate the electrical characteristics, which were fabricated on n-type silicon substrate capped with thermally oxidized SiO_2 layer of 300 nm. To fabricate the memory device, ZnO nanowires were firstly transferred onto the substrate. Then standard photolithography process was utilized to pattern the substrate with ZnO nanowires on top, followed by deposition of 100 nm Ag. Electrical characterization was performed in air at room temperature by using semiconductor parameter analyzer (Agilent 4155C). The transportation of Ag during electrical characterization was confirmed by the mapping of Ag utilizing high spatial resolution Auger electron spectroscopy (HSR-AES). The HSR-AES data was acquired with a PHI 700Xi system utilizing a 20 kV 10 nm electron beam.

5.3 Results and discussion

Figure 4.2 (a) shows a top view SEM image of the as-grown Na-doped ZnO nanowires. The nanowires do not grow vertically on the substrate. The inset shows SIMS result, which indicates that Na was doped into the ZnO nanowires. Figure 4.2 (b) and its inset display a low magnification TEM image of an individual Na-doped ZnO nanowire and its selected area electron diffraction (SAED) pattern, respectively, showing that the Na-doped ZnO nanowire grows along [0001] direction. The representative HRTEM image is shown in Figure 4.2 (c), in which typical single crystalline ZnO structure could be clearly observed, showing that the change of lattice constant by Na doping is below the resolution of HRTEM. Figure 4.2 (d) shows an SEM image of the Ag/Na-doped ZnO nanowire/Ag memory device, in which two Ag active electrodes are used, simplifying the

fabrication procedure greatly in contrast to the process using one active electrode and one inert electrode.

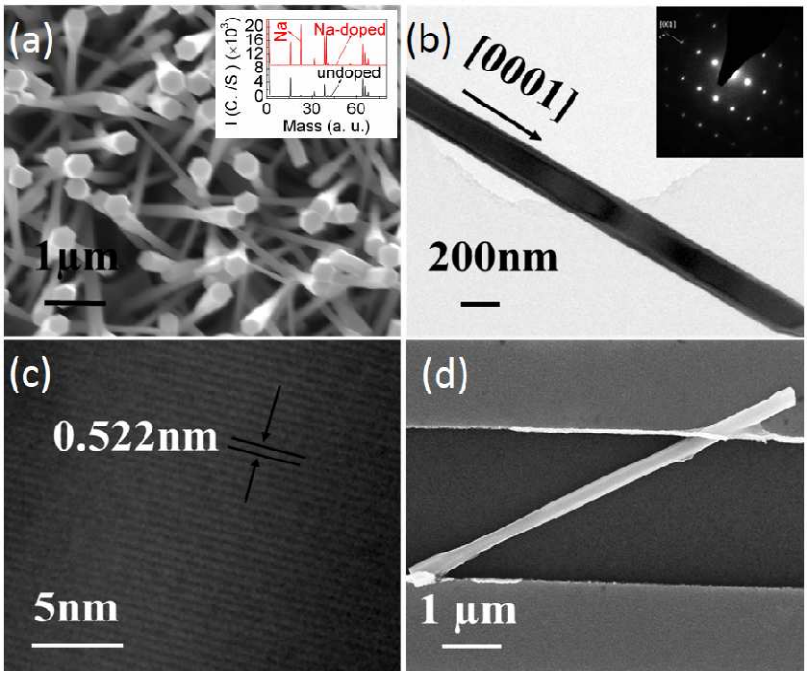

Figure 4.2. (a) SEM image and SIMS spectra (inset) of Na-doped ZnO nanowires. Na was doped into ZnO nanowires, which do not grow vertically on the substrate because of doping. (b) TEM image of a Na-doped ZnO nanowire, inset: SAED pattern of the nanowire. Na-doped ZnO nanowire grows along [0001] direction. (c) HRTEM image of the nanowire in (b). The change of lattice parameters induced by Na-doping is under the resolution of HRTEM. (d) SEM image of the Na-doped ZnO nanowire resistive switching device. Symmetric structure of Ag/nanowire/Ag was used to simplify the fabrication process.

Figure 4.3 (a) and (b) show typical *I-V* characteristics of Na-doped ZnO nanowire device and undoped ZnO nanowire device, respectively. Na-doped ZnO nanowire device shows bipolar resistive switching set and reset at 40V and -40V respectively, which has the self-compliance property with current around 10 μA and self-rectifying property with rectifying ratio of 10^5 at low resistance state (LRS). Undoped ZnO nanowire device shows typical bipolar resistive switching, which needs external current compliance, and is similar to the results reported by Yang *et al* in single crystalline ZnO nanowire electrode by Ag [17]. These results indicate that Na-doping plays important roles in both the self-compliance and self-rectifying properties at LRS. Figure 4.3 (c) and (d) show retention and DC sweeping endurance characteristics of Na-doped ZnO nanowire device, respectively. LRS exhibits no significant degradation after 1×10^5 s, while high resistance state (HRS) shows no degradation. The two states can still be well distinguished by high resistance ratio of over 10^3, as the data trends are extrapolated to 100 years. This result indicates good retention. For endurance, as shown in Figure 4.3 (d), no significant degradation of both LRS and HRS with a large resistance window of over 10^3 can be observed.

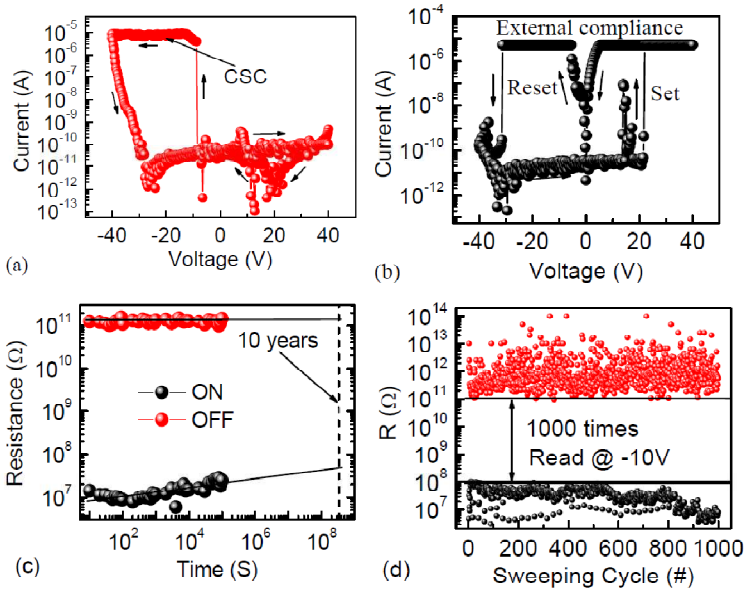

Figure 4.3. (a) Typical I-V characteristics of Na-doped ZnO nanowire device, which shows current self-complianced (CSC) and self-rectified resistive switching behavior set and reset at 40V and -40V, respectively. The self-complianced current is about 10μA and the self-rectifying ratio is 10^5 at low resistive state. (b) Typical non-rectifying I-V characteristics of undopedZnO nanowire device, which needs external compliance. The current self-complianced and self-rectifying properties are due to Na-doping. (c) Retention, and (d) endurance results of resistive switching memory fabricated with Na-doped ZnO nanowire. The two states can still be well distinguished by high resistance ratio of over 10^3, as the data trends are extrapolated to 100 years. Both LRS and HRS with a large resistance window during DC sweeping periods of over 10^3 exhibited little degradation.

After electrical measurements, some white dots were found on the biased side of the nanowire as shown in the SEM image in Figure 4.4 (a), comparing with its SEM image before electrical measurements shown in Figure 4.2 (d). Figure 4.4 (b) shows the corresponding results of HSR-AES Ag map after a layer of 1 nm was sputtered away to avoid contamination. Combining with Zn and O maps shown in Figure 4.5, it is concluded that these white dots are composed of Ag. In addition to these white dots, Ag

also distribute along the whole nanowire. The part with highest Ag content is at the biased end of the nanowire while the lowest one is in the middle. The content of Ag was measured quantitatively choosing 13 points along the nanowire. The results are provided in Figure 4.4 (c), which shows that Ag content at the biased end is much higher than that at the grounded end and the middle. The quantitative contents of Ag were also measured for these 13 points after layers of 2 nm, 3 nm, 5 nm, 10 nm, 20 nm, and 50 nm were sputtered away. Figure 4.4 (d) shows the results. Together with the SEM image and Zn, O, Ag maps shown in Figure 4.6, it indicates that although there are some Ag atoms in the core of the Na-doped ZnO nanowire, Ag mainly distribute on the surface of the nanowire. While for the nanowire without going through electrical characterization, there is no Ag signal along the whole nanowire, as shown in Figure 4.7. According to Figure 4.2 (d), Figure 4.4 and Figure 4.7, Ag atoms were transferred onto the ZnO nanowire during *I-V* characterization. These results indicate that the resistive switching in single Na-doped ZnO nanowire is induced by the formation and rupture of Ag nanoisland chain on the nanowire surface,as observed by Yang *et al* in SiO_2-based resistive switching [18], which is similar to the mechanism reported by Yang *et al* [17].

The random distribution of Na dopants can serve as a load resistor in series to constrain the current [19]. The Ag mobile ions forming the conducting nanoisland chain can be partially retracted from the grounded side of the nanowire surface at small negative biases which suppresses the device conductance and induces the load resistor to be variable with negative bias increases, which is corresponding to the self-compliance behavior. The partial retraction of Ag was also observed in Ag/a-Si/poly-Si system [20].

The self-rectifying behavior of ZnO nanowire can be explained by the asymmetric contacts between ZnO nanowire and Ag electrodes, as reported previously in the structures of Ag/randomly oriented nanorods/Ag [21], Au/aligned nanorods /Au [22], and Au/single nanobelt/Au [23]. In Figure 4.3 (a), the first voltage sweeping process is from 0V to 40V, the *I-V* characteristics of which is similar to a diode with p-type end grounded. When the first voltage sweeping process is from 0V to -40V, the *I-V* characteristics is similar to a diode with n-type side grounded, as shown in Figure 4.8. These results indicate that the direction of the diode is related to the first voltage sweeping process. While in undoped ZnO nanowire, the *I-V* characteristics show no difference using different first voltage sweeps. Because Na is a p-type dopant in ZnO [24], a large amount of electrons in the nanowire are compensated by Na-doping, which makes the nanowire more resistive and the good contact more difficult to obtain, although Na-doped ZnO nanowire is still n-type under the growth condition in this experiment, as shown in Figure 4.9. At the same time Ag can also be utilized as p-type dopant in ZnO nanowire [25] besides forming nanoisland chain on the surface. During the voltage sweeping from 0V to 40V, Ag atoms doped into the nanowire moved towards the grounded side. The biased side was more conductive while the grounded side was more resistive. Finally, a good contact between nanowire and Ag at biased side was formed while that at grounded side kept as Schottky contact. The whole nanowire system can be treated as a resistor in series to a Schottky diode, as shown in the inset of Figure 4.4 (a).

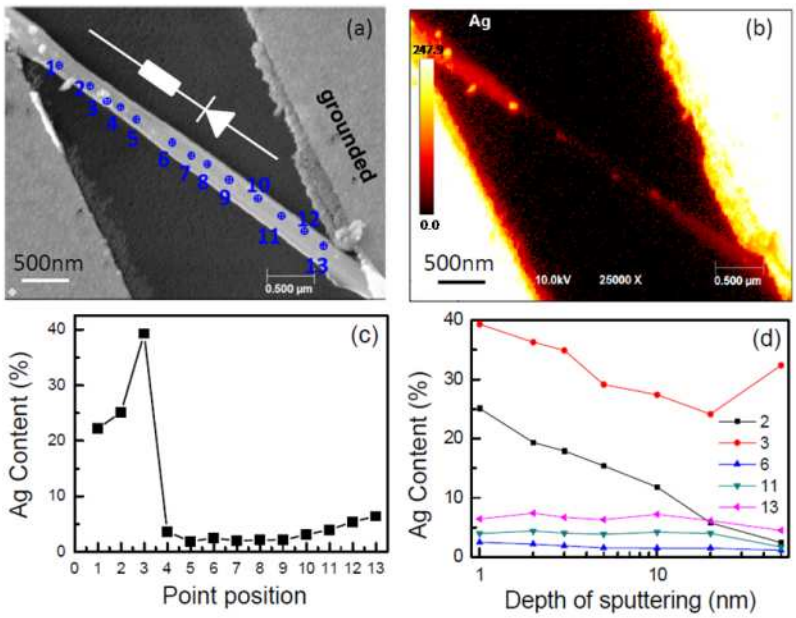

Figure 4.4**.** (a) SEM image and (b) Ag map for the ZnO nanowire resistive switching device. After I-V characterizations, Ag dots show up on the surface of Na-doped ZnO nanowire. Ag contents along the Na-doped nanowire after I-V characteristics (c) on the surface and (d) after layers with different thickness were sputtered away. Ag distributes mainly on surface of the biased side of the Na-doped ZnO nanowire.

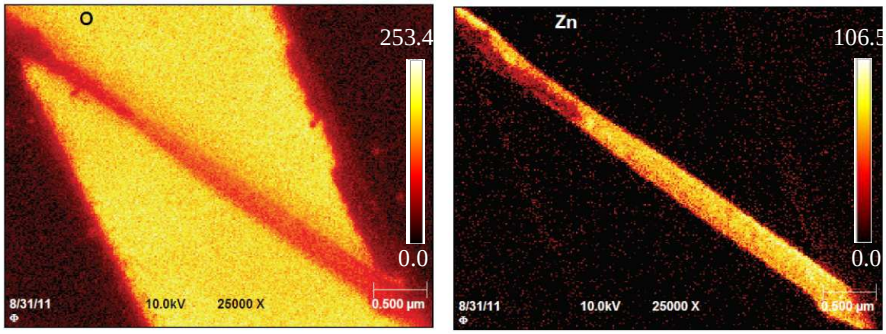

Figure 4.5. AES O and Zn map of ZnO nanowire device after 1nm material on the surface was sputtered away to exclude the effect of possible contamination on mapping.

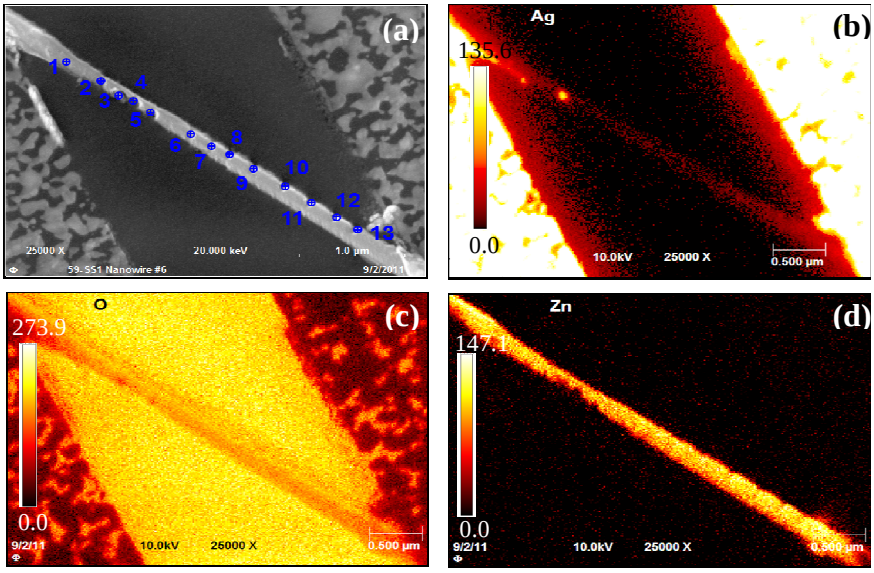

Figure 4.6. (a) SEM image, (b)-(d) Ag, O and Zn map for the measured ZnO nanowire resistive switching device after 50nm material on the surface was sputtered away.

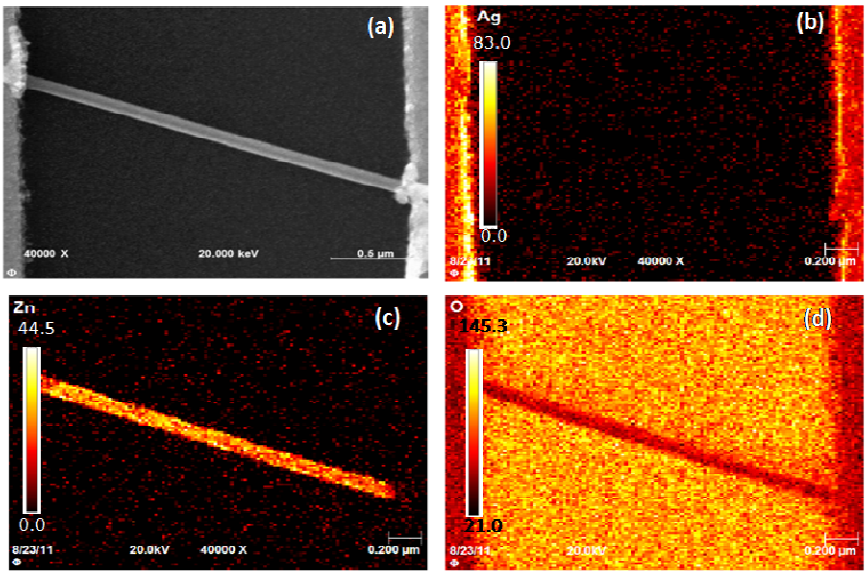

Figure 4.7. (a) Typical SEM image and (b)-(d) Ag, Zn, O maps for ZnO nanowire without going through *I-V* characterizations.

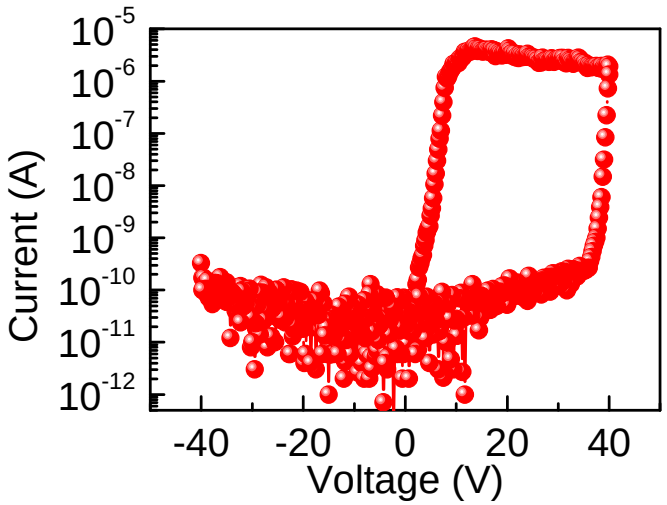

Figure 4.8. *I-V* characteristics for Na-doped nanowire when the first voltage sweeping range is from 0V to -40V.

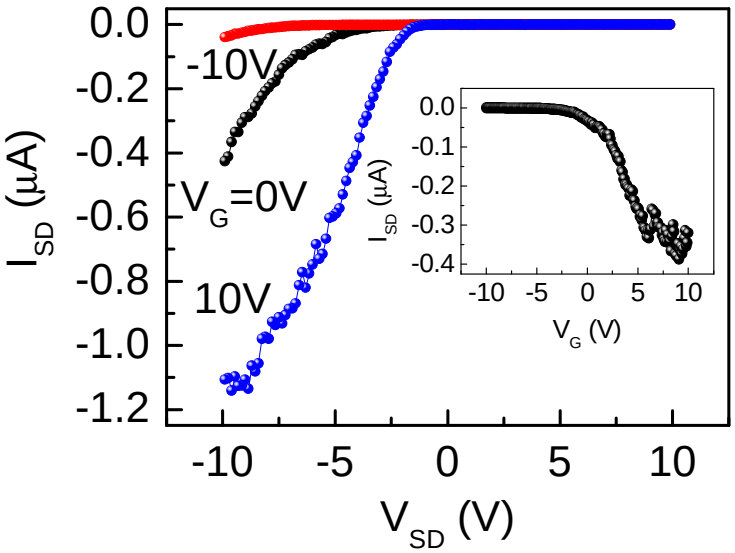

Figure 4.9. I_D-V_D, inset: I_D-V_G results for the FET device fabricated with Na-doped ZnO nanowire, in which Al contact on the back of SiO_2/Si-substrate was utilized as gate.

4.4 Summary

In summary, current self-complianced and self-rectifying bipolar resistive switching was observed in Ag-contacted, Na-doped ZnO nanowire resistive memory. SEM, HSR-AES and I-V characteristics show that the resistive switching was controlled by the formation and rupture of Ag nano-island chain on the surface of the nanowire. The self-compliance is induced by Na-doping and partially retraction of Ag from the nanoisland chain while the self-rectifying behavior is mainly originated from asymmetric contact between nanowire and Ag contact induced by Na-doping and Ag atom segregation and doping. The demonstration of current self-compliance and self rectifying in Na-doped nanowire resistive memory can significantly simplify the future resistive random access memory circuitry because no separate selector device is necessary.

References

[1] A. Asamitsu, Y. Tomioka, H. Kuwahara, Y. Tokura, Nature 1997, 388, 50-52.

[2] R. Waser, M. Aono, Nat. Mater. 2007, 6, 833-840.

[3] M. J. Lee, Y. Park, D. S. Suh, E. H. Lee, S. Seo, D. C. Kim, R. Jung, B. S. Kang, S. E. Ahn, C.-B. Lee, D. H. Seo, Y. K. Cha, I. K. Yoo, J. S. Kim, B. H. Park, Adv. Mater., 2007, 19, 3919-3923.

[4] C. Moreno, C. Munuera, S. Valencia, F. Kronast, X. Obradors, C. Ocal, Nano Lett. 2010, 10, 3828-3835.

[5] J. Borghetti, G. S. Snider, P. J. Kuekes, J. J. Yang, D. R. Stewart, R. S. Williams, Nature 2010, 464, 873-876.

[6] Q. Xia, W. Robinett, M. W. Cumbie, N. Banerjee, T. J. Cardinali, J. J. Yang, W. Wu, X. Li, W. M. Tong, D. B. Strukov, G. S. Snider, G. Medeiros-Ribeiro, R. S. Williams, Nano Lett. 2009, 9, 3640-3645.

[7] L. O. Chua, IEEE Trans. Circuit Theory 1971, 18, 507-519.

[8] L. O. Chua, S. M. Kang, Proc. IEEE 1976, 64, 209-223.

[9] D. B. Strukov, G. S. Sinder, D. R. Stewart, R. S. Williams, Nature 2008, 453, 80-83.

[10] Y. V. Pershin, M. Di Ventra, IEEE Trans. Circuits Syst. I-Reg Papers 2010, 57, 1857-1864.

[11] K. K. Likharev, J. Nanoelectron. Optoelectron. 2008, 3, 203-230.

[12] S. H. Jo, T. Chang, I. Ebong, B. B. Bhadviya, P. Mazumder, W. Lu, Nano Lett. 2010, 10, 1297-1301.

[13] Y. V. Pershin, M. Di Ventra, Neural networks 2010, 23, 881-886.

[14] Q. Zuo, S. Long, Q. Liu, S. Zhang, Q. Wang, Y. Li, Y. Wang, M. Liu, J. Appl. Phys. 2009, 106, 073724-1-073724-5.

[15] Z. Wang, W. G. Zhu, A. Y. Du, L. Wu, Z. Fang, X. A. Tran, W. J. Liu, K. L. Zhang, H.-Y. Yu, IEEE Trans. Electron Dev. 2012, 59, 1203-1208.

[16] K. Kim, S. Gaba, D. Wheeler, J. M. Cruz-Albrecht, T. Hussain, N. Srinivasa, W. Lu, Nano Lett. 2012, 12, 389-395.

[17] Y. Yang, X. Zhang, M. Gao, F. Zeng, W. Zhou, S. Xie, F. Pan, Nanoscale, 3, 2011, 1917-1921.

[18] Y. Yang, P. Gao, S. Gaba, T. Chang, X. Pan, W. Lu, Nat. Comm. 2012, 3, 732-1-732-8.

[19] L. C. Bum, L. D. Soo, A. Benayad, L. S. Ryul, C. Man, L. Myoung-Jae, H. Jihyum, K. C. Jung, U. I. Chung, IEEE Electron Device Lett. 2011, 32, 399-401.

[20] K. Kim, S. Jo, S. Gaba, W. Lu, Appl. Phys. Lett. 2010, 96, 053106-1-053106-3.

[21] S. Bayan, D. Mohanta, Journal of Electronic Materials, 2012, 41, 1955-1961.

[22] O. Harnack, C. Pacholski, H. Weller, A. Yasuda, J. M. Wessels, Nano Letters, 2003, 3, 1097-1101.

[23] C. S. Lao, J. Liu, P. Gao, L. Zhang, D. Davidovic, R. Tummala, Z. L. Wang, Nano Letters, 2006, 6, 263-266.

[24] W. Liu, F. Xiu, K. Sun, Y. Xie, K. L. Wang, J. Zou, Z. Yang, J. Liu, J. AM. Chem. Soc. 2010, 132, 2498-2499.

[25] I. S. Kim, E. K. Jeong, D. Y. Kim, M. Kumar, S. Y. Choi, Applied Surface Science, 2009, 255, 4011

Charpter 5

ZnO p-n homojunction random laser based on nitrogen doped nanowires and undoped thin film

5.1 Introduction

Random lasers, which are based on highly disordered gain medium, have attracted much attention owing to their various potential applications. For example, random lasers are ideal for display applications because they usually exhibit a very broad angular distribution [1]. Besides, they can be used for remote heat sensing [2], document encoding [3], chemical sensing [4], and even medical diagnostics [5,6]. Furthermore, compared with conventional lasers, the unique advantage of random lasers lies in simple structures, which can be realized by cost-effective processing techniques with various materials. The random laser action has been observed in many different structures including nanoparticles [7,8], nanowires [9-11] and thin films [12], and in different materials such as ZnO [12,13], liquid dye [14] and solid state polymer [15].

Among various materials for random lasing, ZnO is a promising material owing to its direct band gap and large exciton binding energy of ~60 meV at room temperature [16]. Its one dimensional structure, which can be synthesized by various low-cost methods, is an excellent optical cavity for random lasers. Many attempts have been made to induce lasing behavior in ZnO nanowire-based devices [17-24]. Nevertheless, most of the random lasers based on ZnO nanowires are induced by optical pumping [17-20]. For

practical laser applications, electrical pumping is needed. Electrically pumped ZnO nanowires random lasers have been demonstrated based on ZnO metal insulator semiconductor structures [21,22] and heterojunctions [23,24], while the nanowires random laser diode based on ZnO p-n homojunction, which can significantly enhance the output power for practical applications, has not been reported yet. The difficulty mainly lies in the problem of p-type doping of ZnO nanowires.

Nitrogen has been reported to be a good p-type dopant for ZnO thin film [25-27], although Lyons et al also predicted that nitrogen doping may not produce p-type ZnO at all [28]. In order to clarify this controversial research topic, tremendous experimental and theoretical studies from many research groups may be necessary. Recently, Yuan et al reported CVD growth of nitrogen doped p-type ZnO nanowires [29]. The nanowires were grown on sapphire substrate by using gold as catalyst. Gold can help the growth of ZnO nanowires, however it may be an p-type dopant or deep-level impurity [30] as the atoms are inadvertently introduced into the nanowires during the growth [31], which complicates the origin of the p-type conductivity. In this research, we grew nitrogen doped p-type ZnO nanowires without metal catalyst on ZnO thin film and formed the p-n homojunction. Based on this structure, we demonstrated electrically pumped ZnO nanowires homojunction random laser device. These results suggest that nitrogen can be an effective p-type dopant for ZnO nanowires.

5.2 Experiments

The undoped ZnO seed layer was grown using plasma-assisted molecular-beam epitaxy. First, a thin MgO buffer layer (about 3 nm) was grown on n-type silicon substrate at 350 °C with a Mg cell temperature of 460 °C. The 400 nm thick undoped ZnO film was then grown at a substrate temperature of 500 °C with a Zn effusion cell temperature of 360 °C. Figure 5.1 shows the top view SEM image of the thin film, which presents columnar structure. Electrical properties of the ZnO film were characterized by Hall effect measurement under a Van der Pauw configuration. Electron concentration of 1.8×10^{18} cm^{-3}, mobility of 4.4 cm^2/Vs and resistivity of 0.80 Ωcm were obtained.

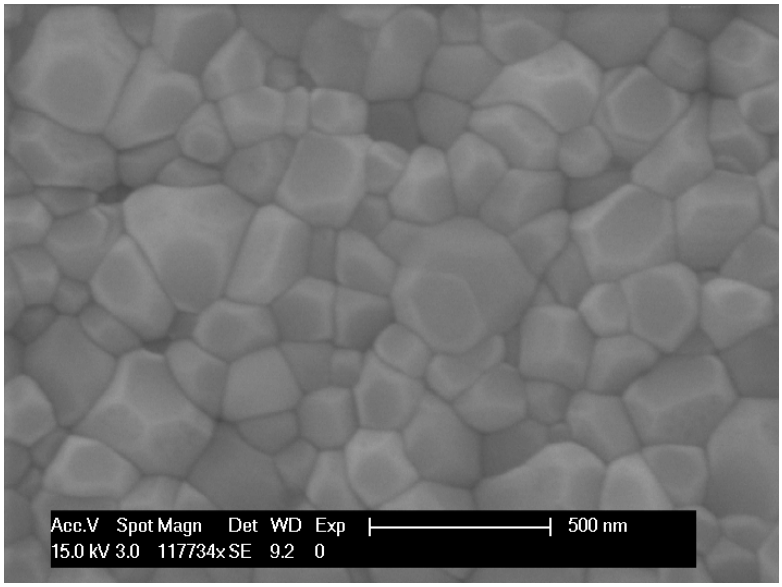

Figure 5.1. SEM image of undoped ZnO thin film. Typical ZnO compact columnar structure on Si is observed.

Nitrogen doped ZnO nanowires were grown in a CVD furnace on a high-quality undoped ZnO seed layer on n-type Si (100) substrate. The 400 nm n-type seed layer was grown on a 3-nm MgO buffer in plasma-assisted molecular beam epitaxy (MBE). To grow nitrogen doped p-type ZnO nanowires, argon diluted oxygen (0.5%) was used as reaction gas and argon diluted N_2O (0.5%) was used as dopant gas. The flow rates were 200 s.c.c.m. and 50 s.c.c.m., respectively. A flow of 1000 s.c.c.m. nitrogen was passed continuously through the furnace during the growth. Zinc powder (99.999% Sigma Aldrich) was placed in a silica bottle and served as source material. The substrate was positioned at the center of the silica tube, which was about 1cm away from the silica bottle at the downstream side. The growth temperature is 650 ℃ and the growth duration is 40 min. Part of the substrate was covered by a piece of silicon wafer during the growth for subsequent electrical contact formation on the ZnO film.

To fabricate the nanowire/thin film laser diode, an ITO glass was clamped on the top end of the nanowires as the top electrode and Ti/Au (10nm/100nm) was deposited on the undoped n-type ZnO as the ground electrode using e-beam evaporation. During the Ti/Au metal evaporation, the nanowires were protected by an aluminum foil.

To fabricate the nanowire back-gated FET, the nitrogen doped ZnO nanowires were transferred onto a SiO_2 (300 nm)/p+-Si wafer and then the Ni/Au electrodes were formed on an individual nanowire by using photolithography and e-beam evaporation. Al was deposited on the back of the silicon wafer to form the back gate electrode.

5.3 Study of p-type nitrogen doped ZnO nanowires

Figure 5.2 (a) and 5.2 (b) show SEM images of the top view and cross sectional view of the nanowires sample, respectively. The average diameter of the nanowires is about 200 nm and the length is about 3.5 μm. From the cross sectional view of the nanowires (Figure 5.2 (b)), it is noticeable that most nanowires are not vertically aligned, but tilted 10-15 degree with respect to the normal of the substrate surface. This may be due to the rough surface of the original ZnO thin film seed.

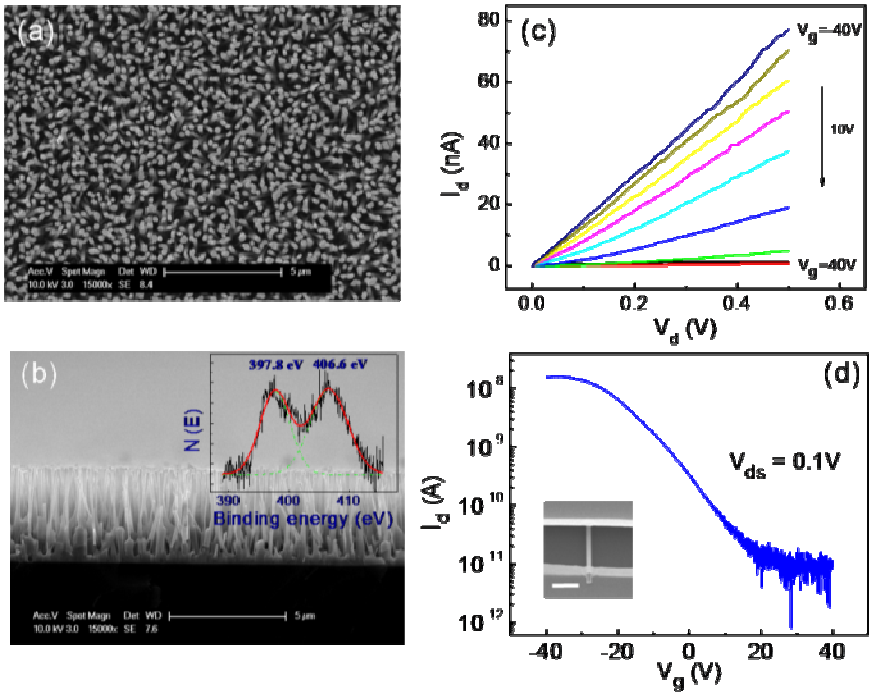

Figure 5.2. (a) Top view SEM image of nitrogen doped ZnO nanowires. The sidewall of the nanowires can be seen, indicating that the nanowires are not totally vertically aligned. (b) Side view SEM image of nitrogen doped ZnO nanowires. Inset: XPS spectrum of the sample. (c) I_d-V_d curves of nitrogen doped ZnO nanowire back-gated FET. V_g increases from -40V to 40V with a 10V step. (d) I_d-V_g curves of nitrogen doped nanowire back-gated FET. Inset: SEM image of the measured FET device. The scale bar is 2 μm.

X-ray photoelectron spectroscopy (XPS) result of nitrogen doped ZnO nanowires is shown in the inset of Figure 5.2 (b). Two N 1s related peaks at 397.8 eV and 406.6 eV are evident. Both peaks have been reported in the p-type nitrogen doped ZnO thin film [32]. The low energy peak at 397.8 eV corresponds to nitrogen substitution on the oxygen site [33], which is the desired process for p-type doping. The peak at 406.6 eV is assigned to be the N 1s binding energy of NO_3^- radical [33,34]. This high-energy peak, which is commonly observed in the oxygen rich compound [33], suggests that these nanowires were grown under an oxygen rich condition [34]. The oxygen rich growth condition can suppress the "intrinsic" donors such as zinc interstitials and oxygen vacancies [35,36] and help achieve p-type conductivity. From the XPS result, the approximate atomic concentration of nitrogen is 0.1%.

To study the electrical transport properties of nanowires, a single nanowire back-gated field effect transistor (FET) was fabricated. Figure 5.2 (c) shows I_d-V_d curves of the FET (an SEM image of the device is shown as an inset in Figure 5.2 (d)). It is clear that all I_d-V_d curves are linear, indicating that Ohmic contacts have been formed between the nitrogen doped ZnO nanowire and Ni/Au electrodes. The I_d-V_d curves show clear field effect characteristic of p-type conductivity: as the gate voltage increases, the conductance of the nanowire decreases. Figure 1d shows transfer characteristic (I_d-V_g) of the device. The curve with an on/off ratio over 100 represents the typical curve for good p-type conductivity in ZnO nanowire. The hole concentration can be calculated by using the equation [37]: $p_0 = \left(\frac{V_{th}}{q}\right)\left(\frac{4}{\pi d^2}\right)\left[\frac{2\pi\varepsilon_0\varepsilon_r}{\ln(4h/d)}\right]$, where ε_0, ε_r, h, d, V_{th} are the dielectric constant in vacuum, dielectric constant of SiO_2 (3.9), thickness of the SiO_2 (300 nm),

diameter of the nanowire (200nm) and threshold voltage of the FET (about 20 V from the I_d-V_g curve), respectively. The hole concentration of the nanowire is calculated to be about $3 \times 10^{17}\ cm^{-3}$. The hole mobility can be estimated by $\mu_m = g_m \left(\frac{L}{V_d}\right) [\frac{\ln(4h/d)}{2\pi\varepsilon_0\varepsilon_r}]$ [37], where g_m is the transconductance and L is the effective length of the nanowire (~3 μm). The mobility is then calculated to be around 1.5 $cm^2/(Vs)$.

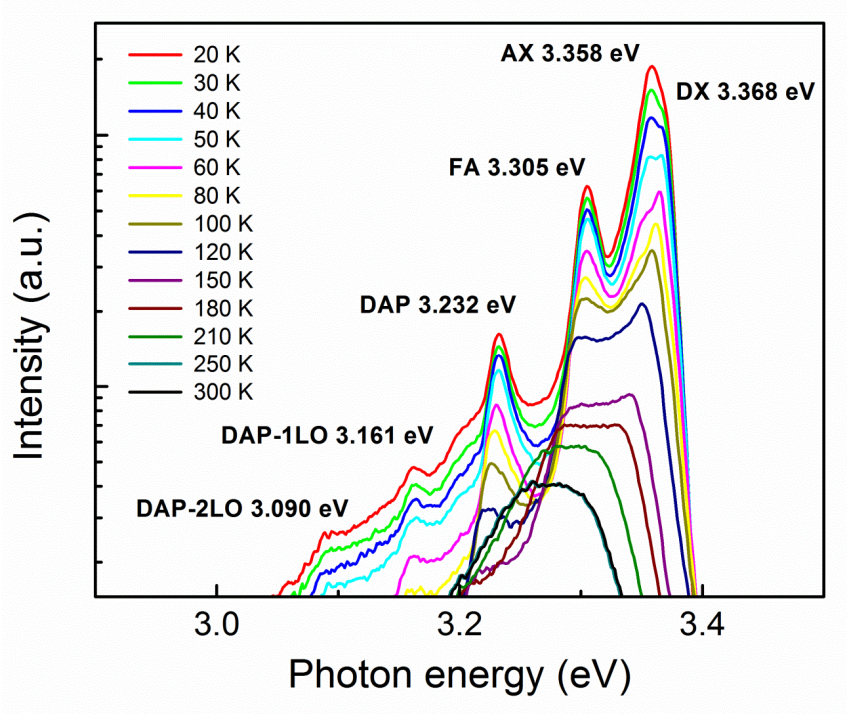

Figure 5.3. Temperature dependent PL spectra of nitrogen doped ZnO nanowires. The temperature ranges from 20 K to 300 K.

The acceptor activation energy is one of the most important parameters to evaluate the p-type dopant in semiconductors and can be extracted by temperature-dependent PL spectra. The p-type characteristic of the nitrogen doped ZnO nanowires in PL is summarized in Figure 5.3. A He-Cd laser with an excitation wavelength of 325nm was used in this experiment. The acceptor bound exciton (*AX*) and donor bound exciton

(*DX*) peaks are at 3.358 eV and 3.368 eV, respectively. The acceptor activation energy ΔE_A for the N(O) acceptor could be derived from the binding energy between the acceptor and free exciton by using Hayne's rule [38]. Figure 5.4 shows the integrated intensity of the *AX* emission shown in Figure 2 as a function of temperature. The intensity follows the equation [39]: $I(T) = I(0)/[1 + Cexp(-E_b^{AX}/kT)]$ (1), where E_b^{AX} is the binding energy of the acceptor and free exciton, and *C* is a fitting parameter. From the fitting (Figure 5.4), $E_b^{AX} = 19.8\, meV$ is obtained. In ZnO, $E_b^{AX}/\Delta E_A \approx 0.1$ [38]. So $\Delta E_A = 198\, meV$.

The peaks at around 3.305 eV and 3.232 eV are due to free electron to acceptor (*FA*) emission and donor-acceptor-pair (*DAP*) emission, respectively [40,41]. The longitudinal-optical (*LO*) phonon replicas of the *DAP* emission are shifted by the ZnO phonon energy of ~71 meV. The activation energy of an acceptor ΔE_A can be calculated with the equation [42] $\Delta E_A = E_{gap} - E_{DAP} - \Delta E_D + < \frac{e^2}{4\pi\varepsilon_0\varepsilon_{ZnO} r_{DAP}} >$. The donor binding energy ΔE_D is reported to be about 30 meV [43-45] and the intrinsic band gap $E_{gap} = 3.435\, eV$ at 20 K [45]. ε_{ZnO} is the dielectric constant of ZnO (8.6). r_{DAP} is the average donor-acceptor pair distance. The last term represents the Coulomb interaction between the donors and acceptors and the value is around 20 meV [42,46]. Based on the assignment of the 3.232 eV peak as the *DAP* transition energy, the acceptor activation energy ΔE_A for the N(O) acceptor is 195 meV.

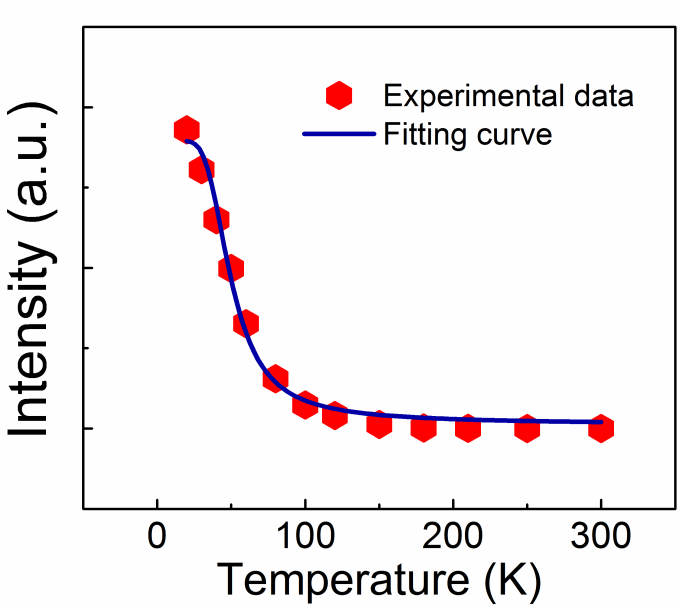

Figure 5.4. Integrated intensity of the *AX* emission as a function of temperature for nitrogen doped ZnO nanowires. The solid line represents the fitting to Eq (1).

In order to get more insight on nitrogen acceptor in the p-type ZnO nanowires, the acceptor activation energy can also be evaluated based on the carrier density approach. From the semiconductor physics, the hole concentration can be calculated by $p_0 = 2\frac{(2\pi m_p^* k_B T)^{3/2}}{h^3} e^{-(E_F - E_v)/k_B T}$ (2), where m_p^* is the effective hole mass ~$0.6m_0$[47]. The occupation probability for acceptor can be described by the Fermi function: $f_A(E) = \frac{1}{\frac{1}{2}e^{(E_F - E_A)/k_B T}+1}$,where E_A is the acceptor energy. In our undoped ZnO nanowires sample (Figure 5.5), the electron concentration is on the order of $10^{17}\ cm^{-3}$, therefore we can reasonably assume a background electron carrier concentration to be between $1 \times 10^{17}\ cm^{-3}$ and $1 \times 10^{18}\ cm^{-3}$ for calculation. Considering the compensation effect, the

activated acceptor concentration ranges from $4 \times 10^{17}\ cm^{-3}$ to $1.3 \times 10^{18}\ cm^{-3}$. The atom density of ZnO is $8.28 \times 10^{22}\ cm^{-3}$ and the nitrogen atomic ratio is 0.1% from the XPS result. So about 0.5%~1.7% of acceptors are activated, which means $f_A(E)$ ranges from 0.995 to 0.983. From the Fermi function, the Fermi energy is $E_F = k_B T ln \frac{2(1-f_A(E))}{f_A(E)} + E_A$. Inserting the Fermi energy into equation (2), and taking T=300 K, the activation energy $\Delta E_A = E_A - E_v$ is between 215 meV and 183 meV, which is in good agreement with the results from PL.

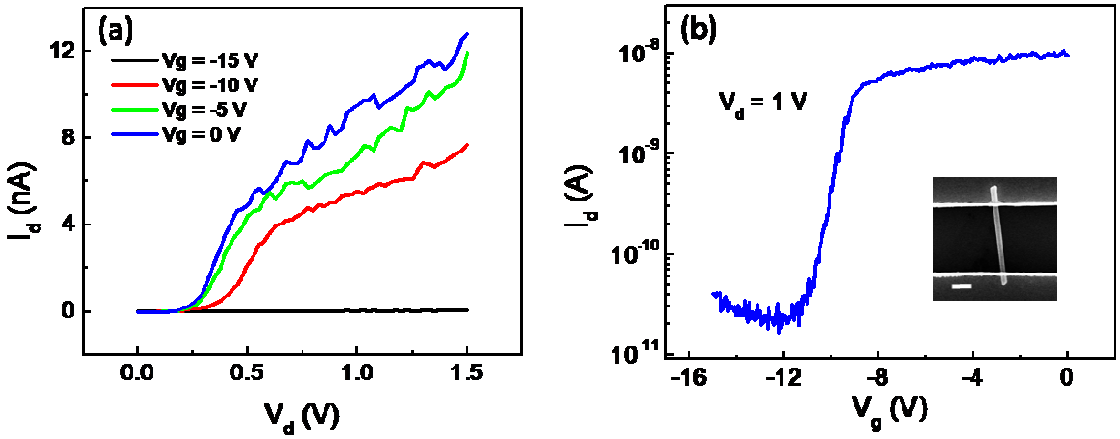

Figure 5.5. (a) I_d-V_d curves of undoped ZnO nanowires back-gated FET. The V_g increases from -15V to 0V with a 5V step. (b) I_d-V_g curves of undoped ZnO nanowires back-gated FET. Inset: SEM image of the measured FET device. The scale bar is 1 μm. The diameter of the nanowire is about 300 nm and the effective length of the device is ~3.5 μm. The I_d-V_d curves show clear field effect characteristic of n-type conductivity: as the gate voltage increases, the conductance of the NW increases. The transfer characteristic I_d-V_g also presents the n-type conductivity, showing a threshold voltage at -12V. Using the approach in the article, the electron concentration and mobility are calculated to be 1.7×10^{17} cm^{-3} and 1.4 cm^2/Vs, respectively.

5.4 P-n homojunction laser device

Figure 5.6 shows the evolution of PL emission spectra of the ZnO nanowires as a function of excitation pumping power at room-temperature. The excitation source in this experiment is a Nd:YAG pulse laser with an output wavelength of 355 nm. The laser has 10 Hz frequency and 3 ns pulse duration. A silicon CCD is used as the detector and the spectrum resolution is 0.054nm. The pumping power ranges from 168 kW/cm^2 to 491 kW/cm^2 with average steps of 30 kW/cm^2. Lasing characteristics are evident from the spectra and the threshold power is found to be at around 300 kW /cm^2 (Figure 5.6 inset). Below the threshold only a single broad spontaneous emission peak is observed. When the pumping power reaches the threshold, a few discrete narrow lasing peaks with linewidth of about 0.4 nm emerge from the single broad spontaneous emission spectrum. At higher pumping powers, more peaks also begin to emerge because more lasing modes are activated. These peaks are not evenly spaced and are not stable, which suggest that the lasing shall originate from random lasing based on the multiple light scattering among the nanowires rather than Fabry-Perot mechanism, where each nanowire serves as gain cavity [48]. The density of electron-hole pairs (n_p) produced by the optical pumping can be calculated by $n_p = I_{exc}\tau/h\omega l$ [49]. Here, I_{exc} is the excitation power, τ is the spontaneous emission lifetime (about 300 ps for ZnO) [50] and l is the diffusion length (about 2 μm for ZnO) [51]. At the threshold pumping power 300 kW /cm^2 , n_p is calculated to be $8.5 \times 10^{17}\ cm^{-3}$. Because Mott density in ZnO has been controversial as seen in between $5 \times 10^{17}\ cm^{-3}$ and $3.7 \times 10^{19}\ cm^{-3}$ [49,52,53], the gain may originate from exciton interaction, or from electron hole plasma, or from both.

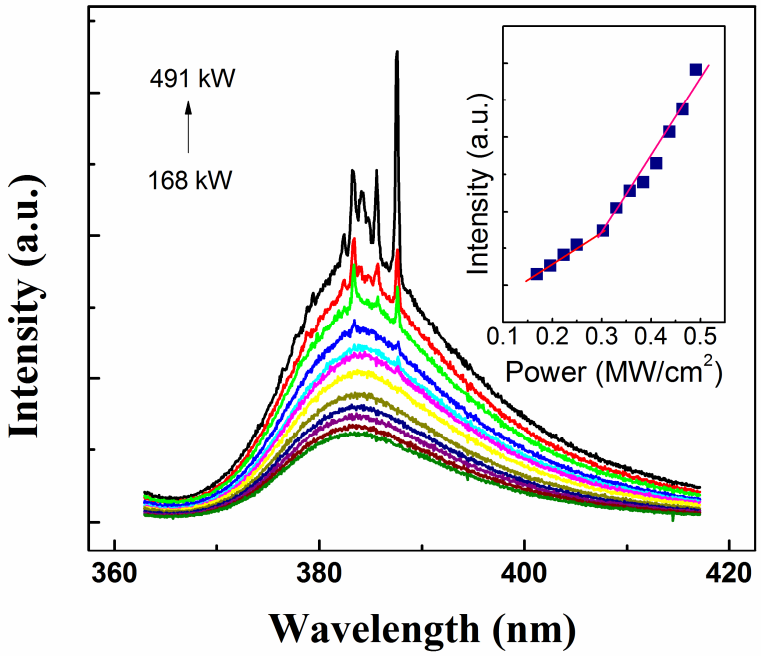

Figure 5.6. Room-temperature optically pumped lasing spectra. Inset: integrated spectra intensity as a function of pumping power density. Solid lines are guide to the eye, indicating threshold power P_{th} (0.3MW/cm^2).

Figure 5.7 (a) shows the schematic of the electrical pumping device. The fabrication of the device is described in the method section. The formation of the ZnO homojunction between the nanowires and thin film was investigated by electron-beam-induced current (EBIC) profiling, which was widely used to investigate the junctions in semiconductors [54,55]. Figure 5.7 (b) shows EBIC profile superimposed on a cross-sectional SEM image. An accelerating voltage of 30 kV was applied, corresponding to the electron penetration depth of 1.5 µm. The EBIC signal forms a clear peak on the ZnO thin film/nanowire junction due to electron-hole pairs from electron beam irradiation generation drifted by built-in electric field in the p-n junction depletion region. The inset

of Figure 5.7 (b) shows current-voltage (I-V) characteristic of the ZnO p-n junction. Rectifying behavior is clearly observed. Both I-V and EBIC results indicate the formation of ZnO nanowire/ZnO thin film p-n homojunction.

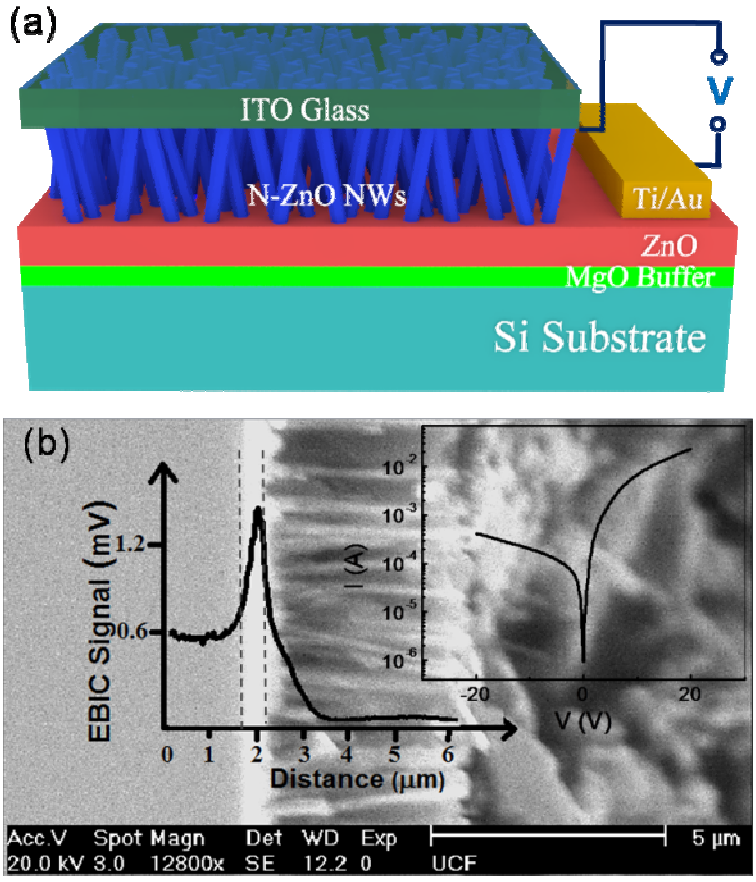

Figure 5.7. (a) Schematic of the electrically pumped laser device. (b) EBIC profile superimposed on the side-view SEM image of the cleaved device. Inset: I-V characteristic of the ITO/ZnO nanowire/ZnO/Ti/Au film laser device. The Ti/Au contact is grounded.

Figure 5.8 (a)-(c) show electroluminescence (EL) spectra of the device with the increase of drive current. The detector was placed perpendicular to the sample surface. As can be seen from Figure 5.8 (a), for the current below 40 mA, the EL emission is

relatively weak and the spectrum is greatly spoiled by noise. At 40 mA, a single broad spontaneous emission peak centered at around 388 nm appears, which is ascribed to the near band edge UV emission from ZnO. As the current increases further (50 mA), a few randomly distributed narrow peaks appear in the spectrum. The lasing peaks become stronger and sharper and more peaks show up as the current reaches 60 mA (Figure 5.8 (b)) and 70 mA (Figure 5.8 (c)). The linewidth of these peaks is less than 2 nm. The detected output power as a function of injection current is shown in the inset of Figure 5.8 (a). The output power was measured using a Thorlabs PM100 Optical Power Meter. The solid lines are the guide to the eye, showing the threshold current of ~40 mA. The output power is about 70 nW at 70 mA drive current. The detector cannot receive all the light from the device, and just part of the power has been detected, leading to this relatively low output power. However, this value is already over one order of magnitude higher than that of the metal oxide semiconductor random laser structure reported [21]. As seen from the EL spectra, the spacing between the adjacent sharp peaks is not uniform and the peak positions between different measurements are different. Therefore, the lasing peaks in the EL spectra should be related to the random lasing instead of F-P lasing. These multiple sharp peaks in the spectra between 370 nm and 410 nm represent different lasing modes of the nanowires. The far field microscope top view images and side view images (inset) of the laser at different injection current were taken by the commercial digital camera (Figure 5.9). Randomly distributed bright spots can be seen from the top view images. As the drive current increases, more bright emission spots are observed and the luminance becomes higher and higher.

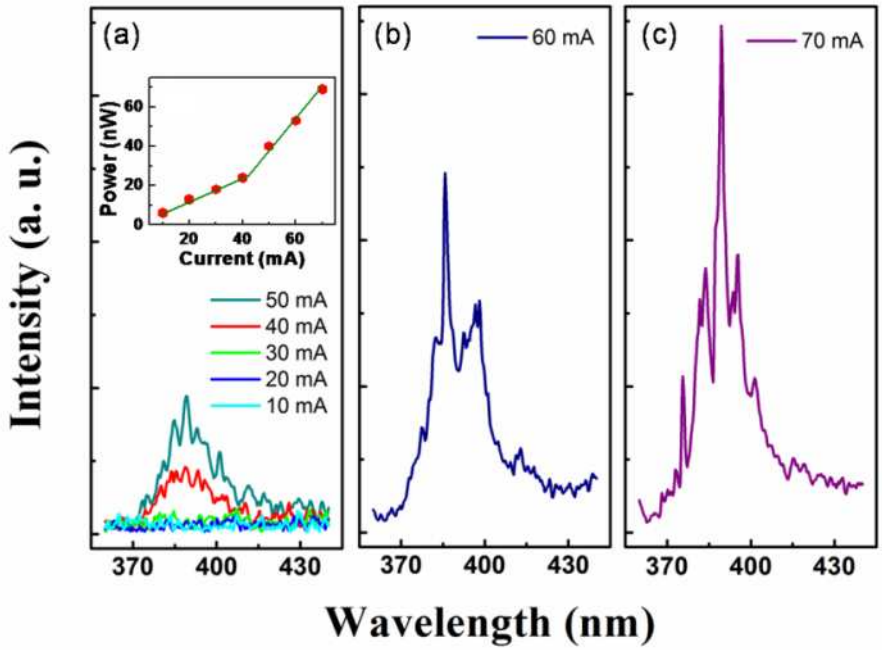

Figure 5.8. Lasing characterization of the device by electrical pumping. EL spectra of the laser device operated at the drive current from (a) 10 mA to 50 mA, (b) 60 mA and (c) 70 mA. Inset of (a) is the output power as a function of drive current.

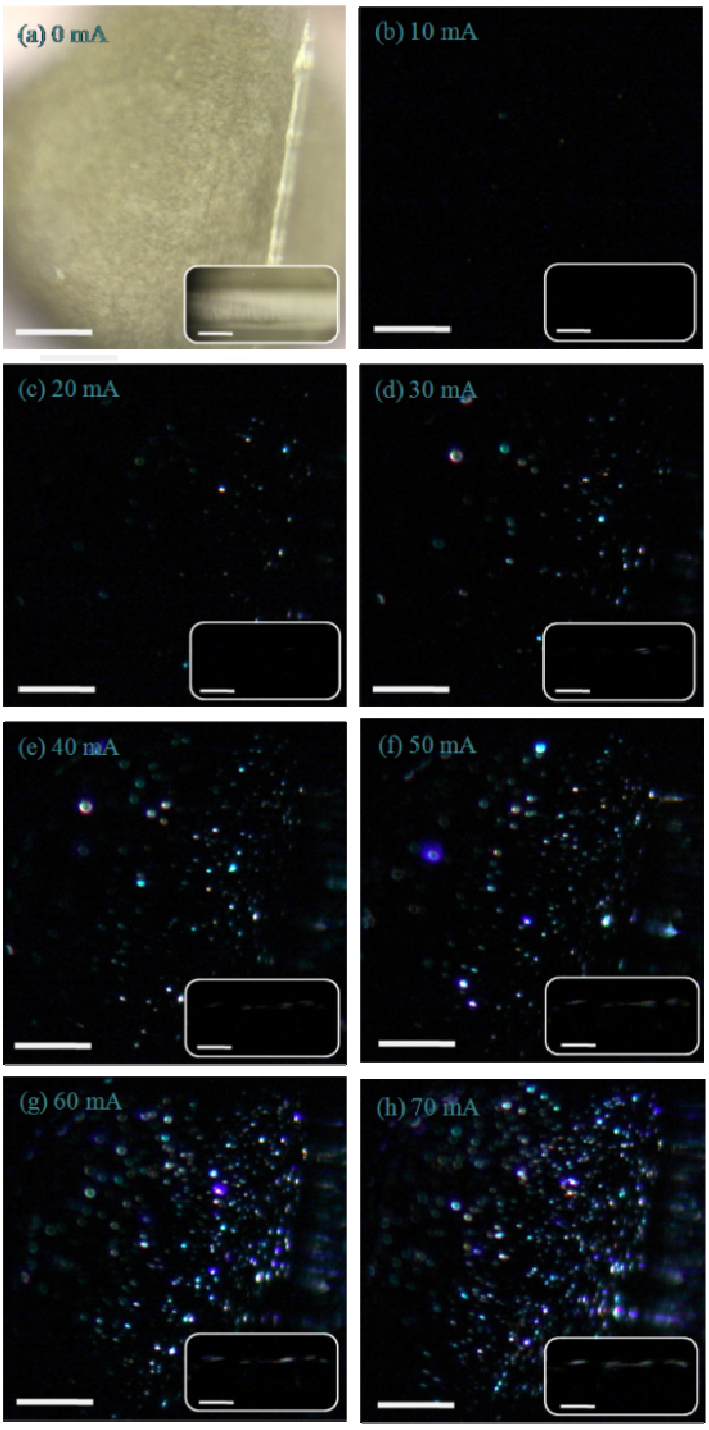

Figure 5.9. Optical microscope images of the lasing device with different drive current. The first image was taken with lamp illumination and zero current injection. The inset of each image is the corresponding side-view microscope image of the device. All the scale bars are 300 μm.

Figure 5.10 shows lasing emission spectra at different observation angles. The injection current is the same for all spectra at 70 mA. The bottom inset in Figure 5.10 is a schematic of the measurement setup. The θ is defined as the observation angle between the detector and sample surface. As shown in Figure 5.10, the laser emission spectra varied drastically with the observation angle. The spectra from different angles show different lasing peaks and different intensities. This is because for a random laser, different random cavities emit the lasing signals in different directions, and the detector placed at a certain angle can only collect the laser signals along its corresponding direction. The top inset in Figure 5.10 shows the integrated spectra intensity versus angle θ. The intensity has a broad distribution and the maximum intensity shows up at θ = 50 degree. Because the nanowires are not totally vertically aligned, the top facets of the nanowires are not in parallel with the interface between ZnO and silicon substrate. Thus, F-P cavity cannot be formed and the lasing signals should originate from the random scattering among the ZnO nanowire arrays. The non-homogeneity in the lasing emission profile, which has been reported in nanopowders and nanowires [56, 57], should be induced by the random tilted angle of the nanowires in our sample.

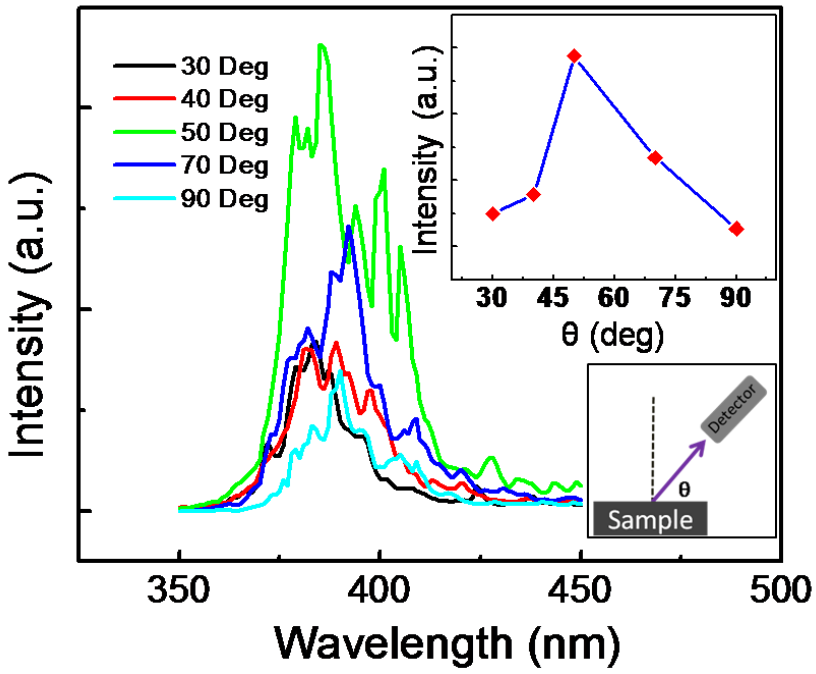

Figure 5.10. Angle dependent EL of the device. Top inset is the integrated spectra intensity as a function of angle. Bottom inset shows the schematic of measurement setup. θ is the angle between the sample surface and detector.

5.5 Summary

In summary, p-type nitrogen doped ZnO nanowires were grown by using CVD without any metal catalyst on ZnO seed layer on silicon substrate. The p-type behavior was studied by the output characteristic and transfer characteristic of the nanowire back-gated FET and PL. An acceptor activation energy of ~200meV was obtained from PL and carrier concentration statistics. The formation of the p-n junction was confirmed by I-V and EBIC results. The lasing behaviors were studied by using both optical pumping and electrical pumping. Above the threshold pumping power/current, random lasing actions

featuring a series of lasing peaks in the spectra were observed. The output power of the electrically pumped laser was measured to be 70 nW at a drive current of 70 mA. The angle dependant EL result shows that the emission has a broad angle distribution, further indicating the formation of ZnO nanowires p-n homojunction random laser.

References

[1] D. S. Wiersma, *Nature Physics* **2008**, *4*, 359 – 367.

[2] D. S. Wiersma, S. Cavalieri, *Nature* **2001**, *414*, 708.

[3] R.M. Balachandran, D.P. Pacheco, N.M. Lawandy, *Appl. Opt.* **1996**, *35*, 640-643.

[4] Q. Song, S. Xiao, Z. Xu, V. M. Shalaev, Y. L. Kim, *Opt. Lett.* **2010**, *35*, 2624-2626.

[5] R. C. Polson, Z. V. Vardeny, *Appl. Phys. Lett.* **2004**, *85*, 1289-1291.

[6] Q. Song, Z. Xu, S. H. Choi, X. Sun, S. Xiao, O. Akkus, Y. L. Kim, *Biomed. Opt. Express* **2010**, *1*, 1401-1407.

[7] S. García-Revilla, M. Zayac, R. Balda, M. Al-Saleh, D. Levy, J. Fernández, *Opt. Express* **2009**, *17*, 13202-13215.

[8] X. Meng, K. Fujita, S. Murai, T. Matoba, K. Tanaka, *Nano Lett.* **2011**, *11*, 1374-1378.

[9] V. V. Zalamai, V. V. Ursaki, C. Klingshirn, H. Kalt, G. A. Emelchenko, A. N. Redkin, *Appl. Phys. B: Lasers Opt.* **2009**, *97*, 817-823.

[10] M. L. Lu, H. Y. Lin, T. T. Chen, Y. F. Chen, *Appl. Phys. Lett.* **2011**, *99*, 091106.

[11] R. Chen, M. I. B. Utama, Z. P. Peng, B. Peng, Q. H. Xiong, H. D. Sun, *Adv. Mater.* **2011**, *23*, 1404-1408.

[12] S. Chu, M. Olmedo, Z. Yang, J. Kong, J. Liu, *Appl. Phys. Lett.* **2008**, *93*, 181106.

[13] H. K. Liang, S. F. Yu, H. Y. Yang, *Appl. Phys. Lett.* **2010**, *97*, 241107.

[14] D. S. Wiersma, S. Cavalieri, *Phys. Rev. E* **2002**, *66*, 056612.

[15] T. Zhai, X. Zhang, Z. Pang, X. Su, H. Liu, S. Feng, L. Wang, *Nano Lett.* **2011**, *11*, 4295-4298.

[16] E. O. Kane, *Phys. Rev. B* **1978**, *18*, 6849.

[17] H. C. Hsu, C. Y. Wu, W. F. Hsieh, *J. Appl. Phys.* **2005**, *97*, 064315.

[18] H. Y. Yang, S. F. Yu, H. K. Liang, C. Pang, B. Yan, T. Yu, *J. Appl. Phys.* **2009**, *106*, 043102.

[19] J. Fallert, R. J. B. Dietz, M. Hauser, F. Stelzl, C. Klingshirn, H. Kalt, *J. Lumin.* **2009**, *129*, 1685-1688.

[20] Y. Chen, Y. Chen, *Opt. Express* **2011**, *19*, 8728-8734.

[21] X. Ma, J. Pan, P. Chen, D. Li, H. Zhang, Y. Yang, D. Yang, *Opt. Express* **2009**, *17*, 14426.

[22] X. Y. Liu, C. X. Shan, S. P. Wang, Z. Z. Zhang, D. Z. Shen, *Nanoscale* **2012**, *4*, 2843-2846.

[23] K. Kim, T. Moon, J. Kim, S. Kim, *Nanotechnology* **2011**, *22*, 245203.

[24] J. Y. Zhang, Q. F. Zhang, T. S. Deng, J. L. Wu, *Appl. Phys. Lett.* **2009**, *95*, 211107.

[25] A. Tsukazaki, A. Ohtomo, T. Onuma, M. Ohtani, T. Makino, M. Sumiya, K. Ohtani, S. F. Chichibu, S. Fuke, Y. Segawa, H. Ohno, H. Koinuma, M. Kawasaki, *Nature Mater.* **2005**, *4*, 42-46.

[26] D. C. Look, D. C. Reynolds, C. W. Litton, R. L. Jones, D. B. Eason, G. Cantwell, *Appl. Phys. Lett.* **2002**, *81*, 1830-1832.

[27] C.C. Lin, S. Y. Chen, S. Y. Cheng, H. Y. Lee, *Appl. Phys. Lett.* **2004**, *84*, 5040.

[28] J. L. Lyons, A. Janotti, C. G. Van de Walle, *Appl. Phys. Lett.* **2009**, *95*, 252105.

[29] G. D. Yuan, W. J. Zhang, J. S. Jie, X. Fan, J. A. Zapien, Y. H. Leung, L. B. Luo, P. F. Wang, C. S. Lee, S. T. Lee, *Nano Lett.* **2008**, *8*, 2591-2597.

[30] Y. Yan, M. M. Al-Jassim, S. H. Wei, *Appl. Phys. Lett.* **2006**, *89*, 181912.

[31] J. S. Lee, M. S. Islam, S. Kim, *Nano Lett.* **2006**, *6*, 1487-1490.

[32] M. Joseph, H. Tabata, T. Kawai, *Jpn. J. Appl. Phys.* **1999**, *38*, L1205-L1207.

[33] C. L. Perkins, S. H. Lee, X. Li, S. E. Asher, T. J. Coutts, *J. Appl. Phys.* **2005**, 97, 034907.

[34] J. Torres, C. C. Perry, S. J. Bransfield, D. H. Fairbrother, *J. Phys. Chem. B* **2003**, *107*, 5558-5567.

[35] D. C. Look, J. W. Hemsky, J. R. Rizelove, *Phys. Rev. Lett.* **1999**, *82*, 2552.

[36] S. B. Zhang, S. H. Wei, A. Zunger, *Phys. Rev. B* **2001**, *63*, 075205.

[37] G. Wang, S. Chu, N. Zhan, Y. Lin, L. Chernyak, J. Liu, *Appl. Phys. Lett.* **2011**, *98*, 041107.

[38] F. X. Xiu, Z. Yang, L. J. Mandalapu, D. T. Zhao, J. L. Liu, *Appl. Phys. Lett.* **2005**, *87*, 252102.

[39] M. Leroux, N. Grandjean, B. Beaumont, G. Nataf, F. Semond, J. Massies, P. Gibart, *J. Appl. Phys.* **1999**, *86*, 3721.

[40] F. Reuss, C. Kirchner, T. Gruber, R. Kling, S. Maschek, W. Limmer, A. Waag, P. Ziemann, *J. Appl. Phys.* **2004**, *95*, 3385.

[41] S. Karamat, R. S Rawat, T. L. Tan, P. Lee, S. V. Springham, E. Ghareshabani, R. Chen, H.D. Sun, *Appl. Surf. Sci.* **2011**, *257*, 1979-1985.

[42] D. C. Look, B. Claflin, *Phys. Stat. Sol. B* **2004** , *241*, 624-630.

[43] D. C. Look, G. C. Farlow, P. Reunchan, S. Limpijumnong, S. B. Zhang, K. Nordlund, *Phys. Rev. Lett.* **2005**, *95*, 225502.

[44] V. Avrutin, D. J. Silversmith, H. Morkoc, *Proc. IEEE* **2010**, *98*, 1302-1315.

[45] B. K. Meyer, H. Alves, D. M. Hofmann, W. Kriegseis, D. Forster, F. Bertram, J. Christen, A. Hoffmann, M. Straßburg, M. Dworzak, U. Haboeck, A. V. Rodina, *Phys. Stat. Sol. B* **2004**, *241*, 231-260.

[46] A. Zeuner, H. Alves, D. M. Hofmann, B. K. Meyer, A. Hoffmann, U. Haboeck, M. Strassburg, M. Dworzak, *Phys. Stat. Sol. B* **2002**, *234*, R7-R9.

[47] N. N. Syrbu, I. M. Tiginyanu, V. V. Zalamai, V. V. Ursaki, E. V. Rusu, *Physica B* **2004**, *353*, 111–115.

[48] S. Chu, G. Wang, W. Zhou, Y. Lin, L. Chernyak, J. Zhao, J. Kong, L. Li, J. Ren, J. Liu, *Nat. Nanotechnol.* **2011**, *6*, 506.

[49] C. Klingshirn, R. Hauschild, J. Fallert, H. Kalt, *Phys. Rev. B* **2007**, *75*, 115203.

[50] D. C. Reynolds, D. C. Look, B. Jogai, J. E. Hoelscher, R. E. Sherriff, M. T. Harris, M. J. Callahan, *J. Appl. Phys.* **2000**, *88*, 2152-2153.

[51] O. Lopatiuk-Tirpak, L. Chernyak, F. X. Xiu, J. L. Liu, S. Jang, F. Ren, S. J. Pearton, K. Gartsman, Y. Feldman, A. Osinsky, P. Chow, *J. Appl. Phys.* **2006**, *100*, 086101.

[52] M. A. M. Versteegh, T. Kuis, H. T. C. Stoof, J. I. Dijkhuis, *Phys. Rev. B* **2011**, *84*, 035207.

[53] Y. Chen, N. T. Tuan, Y. Segawa, H. J. Ko, S. K. Hong, T. Yao, *Appl. Phys. Lett.* **2001**, *78*, 1469.

[54] S. Hoffmann, J. Bauer, C. Ronning, Th. Stelzner, J. Michler, C. Ballif, V. Sivakov, S. H. Christiansen, *Nano Lett.* **2009**, *9*, 1341.

[55] O. Lopatiuk-Tirpak, L. Chernyak, L. Mandalapu, Z. Yang, J. L. Liu, K. Gartsman, Y. Feldman, Z. Dashvsky, *Appl. Phys. Lett.* **2006**, *89*, 142114.

[56] H. Cao, Y. G. Zhao, H. C. Ong, R. P. H. Chang, *Phys. Rev. B,* **1999**, *59*, 15107-15111.

[57] M. A. Zimmler, F. Capasso, S. Muller, C. Ronning, *Semicond. Sci. Technol*. **2010**, *25*, 024001.

Chapter 6

Distributed Bragg reflector assisted low threshold ZnO random laser diode

6.1 Introduction

Random lasers have attracted much attention owing to their various potential applications such as imaging, sensing and medical diagnostics [1-3]. ZnO nanowire is considered to be an excellent random lasing medium due to its large refractive index and exciton binding energy [4]. In addition to Fabry-Perot (F-P) laser [5,6], the electrically pumped ZnO nanowire random laser, which is critical for practical applications, has been demonstrated mainly based on p-n junctions [7] and metal insulator semiconductor structures [8-10]. Nevertheless, the threshold current of these electrically pumped lasers is still too high and needs to be decreased [11,12]. On the other hand, the output power of the electrically pumped nanowire random laser devices also needs to be increased. To achieve these goals, one way is to reduce the loss at the light reflection or scattering. Distributed Bragg reflector (DBR) structures, which are formed from multiple layers of alternating materials with different refractive index and have high reflectivity, can significantly reduce the threshold pumping density and enhance laser performance [13,14]. Here, we demonstrated low threshold DBR-assisted ZnO nanowire random laser device with a p-n homojunction. The output power is also significantly enhanced with the assistance of DBR.

6.2 Experiments

The devices structure consists of nitrogen doped p-type ZnO nanowires/ n-type ZnO thin film/ SiO_2/SiN_x DBR on Si (100) substrate. The 10-period 60.9 nm SiO_2 / 48.7 nm SiN_x DBR structure was grown by plasma enhanced chemical vapor deposition (CVD). Both calculation and experiment results show that the DBR gives desirable optical quality and the reflectivity at 380-390 nm reaches 95%. Details can be found elsewhere [14]. After the DBR deposition, the substrate was immediately transferred to a molecular beam epitaxy (MBE) system, and a 500 nm undoped n-type ZnO seed layer was grown. To grow nitrogen doped p-type ZnO nanowires, 200 s.c.c.m argon diluted oxygen (0.5%) as reaction gas and 50 s.c.c.m argon diluted N_2O (0.5 %) as dopant gas was introduced into a CVD furnace. A flow of 1000 s.c.c.m. nitrogen carrier gas was passed continuously through the furnace during the growth. Zinc (Zn) powder (99.999 % Sigma Aldrich) was placed in a silica bottle and served as source material. The substrate was positioned at the center of the silica tube, which was about 1 cm away at the downstream side from the Zn silica bottle. The growth temperature is 650 ℃. A piece of silicon wafer was used to cover a portion of the substrate during the growth for subsequent electrical contact formation on the ZnO thin film.

6.3 Results and discussion

Figure 6.1 (a) shows the top view scanning electron microscope (SEM) image of the ZnO seed layer. The film consists of compact columnar structures. Figure 6.1 (b)

shows x-ray diffraction (XRD) spectrum of the seed layer, indicating these columns grown preferentially growth along the c-direction of the ZnO wurtzite lattice. The morphology of the seed layer is desirable for subsequent growth of nanowires.

Figure 6.2 (a) and (b) show the top view and side view SEM images of the as-grown nanowires. Tilted nanowires with different diameters from 100 nm to 600 nm are observed. The average length of the nanowires is about 9 μm, although the length of nanowires varies. The size nonuniformity of the nanowires should result from rough surface of the columnar ZnO seed layer on DBR structure.

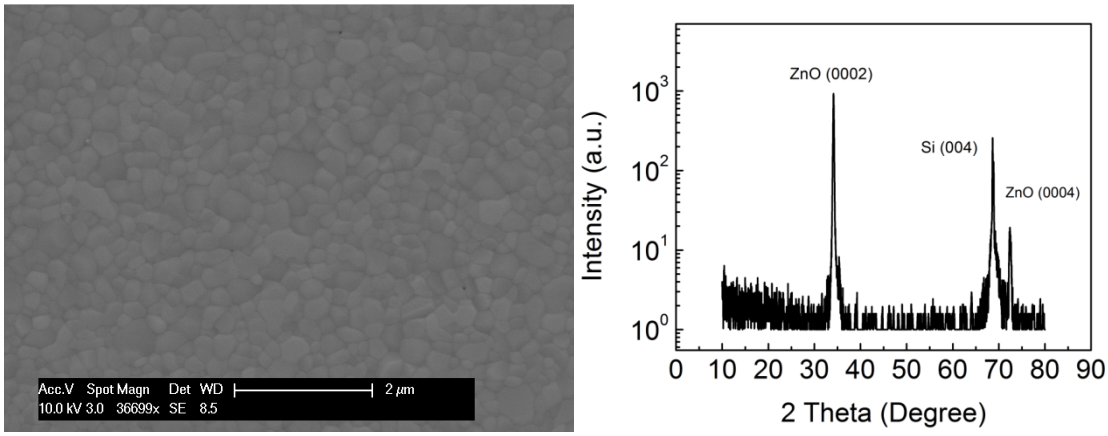

Figure 6.1. (a) SEM image of ZnO seed layer on DBR. (b) XRD result of the seed layer.

Figure 6.3 shows x-ray photoelectron spectroscopy (XPS) result of nitrogen doped ZnO nanowires. Two N 1s related peaks at around 397.8 eV and 406.8 eV are evident. Similar peaks were observed in the previous work [7], which confirms the doping of nitrogen and indicates possible origin of nitrogen related shallow acceptors [15]. From the XPS result, the approximate atomic concentration of nitrogen is 0.1%.

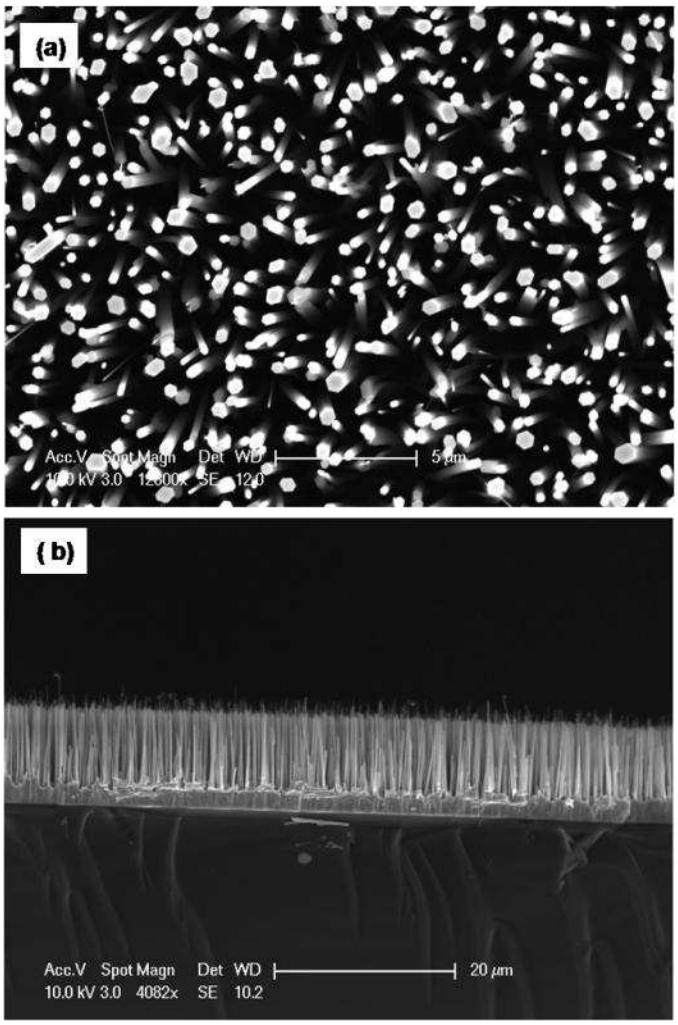

Figure 6.2. Top view (a) and cross-section view (b) of nitrogen doped ZnO nanowires on ZnO seed layer on DBR. The nanowires are slight tilted.

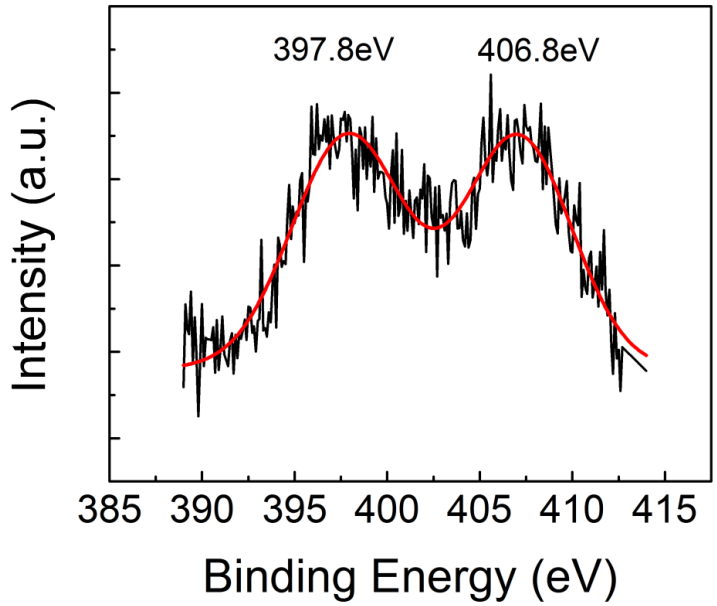

Figure 6.3. XPS result showing nitrogen peaks for nitrogen doped ZnO nanowires.

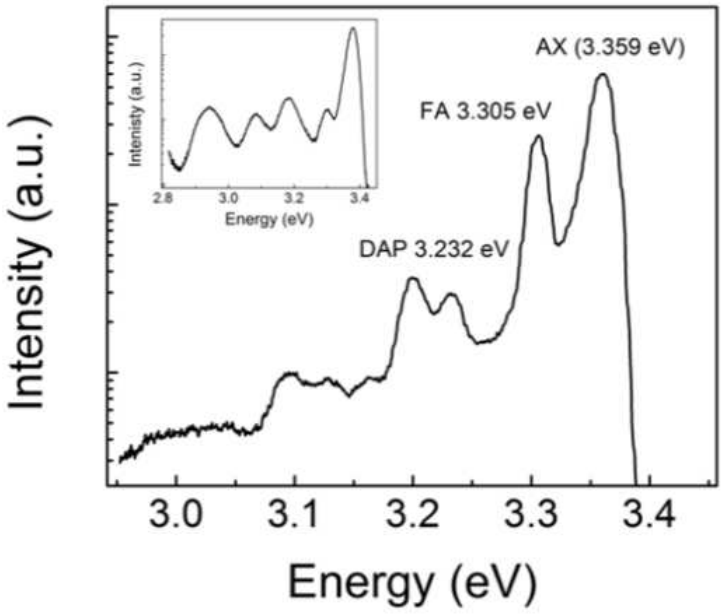

Figure 6.4. Low-temperature PL (20K) for nitrogen doped ZnO nanowires. The inset is the Low-temperature PL (20K) for undoped ZnO seed layer on DBR.

Figure 6.4 shows low-temperature photoluminescence (PL) spectrum of the nitrogen doped ZnO nanowires at 20 K . A He-Cd laser with an excitation wavelength of 325 nm was used in this experiment. The acceptor bound exciton (*AX*), free electron to acceptor (*FA*) emission and donor-acceptor-pair (*DAP*) emission peaks are observed at 3.359 eV, 3.305 eV and 3.232 eV, respectively. Comparing to the reported PL spectrum of nitrogen doped p-type ZnO nanowires [7], additional peaks are observed in the PL spectrum of this sample, which originate from the PL oscillations due to the DBR structure [16]. The similar additional peaks are also observed in the sample with only ZnO seed layer on DBR (Figure 6.4 inset).

The schematic of the device is shown in Figure 6.5. The ITO glass was clamped on the top end of the nanowires as the top electrode. Ti/Au (10 nm / 100 nm) was deposited on the undoped n-type ZnO thin film as the ground electrode using e-beam evaporation. During the Ti/Au metal evaporation, the nanowires were protected by an aluminum foil. Figure 6.6 shows current-voltage (I-V) characteristics of the ZnO p-n junction device with and without UV illumination. The UV illumination was carried out using an Oriel Xe arc lamp. I-V curve in dark exhibits rectifying behavior, which confirms the formation of nitrogen doped ZnO nanowire/ undoped ZnO thin film p-n homojunction. The turn-on voltage is at around 5.5V. Very good UV response in the reverse biased regime can be clearly seen from Figure 6.6.

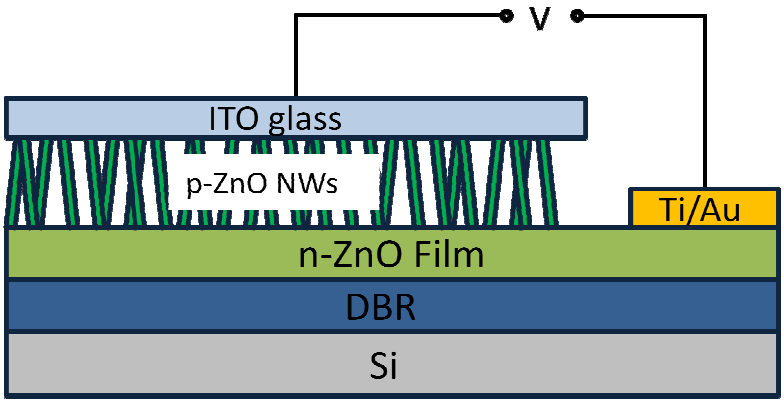

Figure 6.5. Schematic of device structure.

Photocurrent (PC) at different wavelengths was measured using a homebuilt system. An Oriel Xe arc lamp was used as the UV source. The light from the lamp passed through an Oriel 0.25 m monochromator and a specific wavelength light came out from its output port. The light was then cast on the device after chopping. The generated PC signal was collected by a lock-in amplifier. Figure 6.7 shows the PC spectra of the device operated at 0V and different reversed biases. The peaks of the response current are at about 380 nm (3.26 eV), which corresponds to the band gap of ZnO. The PC is a result of the photocarriers generated by the absorption of light in the space-charge region. The PC increases with the increase of the revise bias due to the enhancement of carrier generation from increased space-charge region. These results further confirm the formation of the p-n junction.

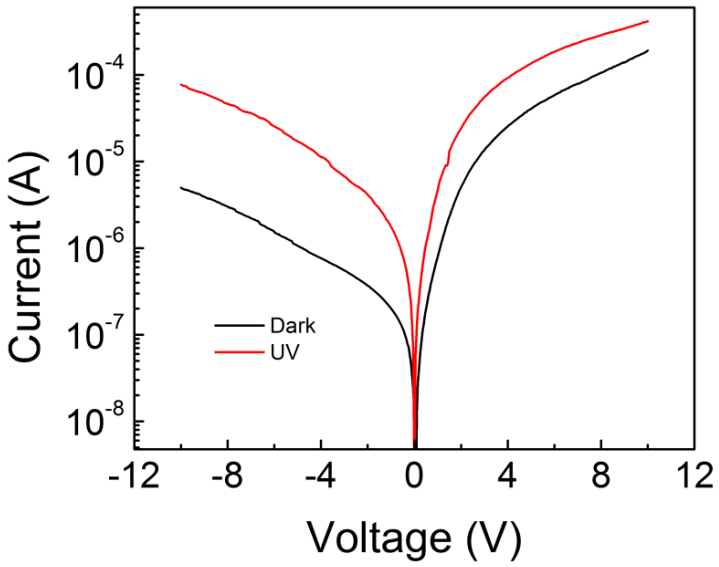

Figure 6.6. I-V characteristics of the ZnO nanowire/ZnO thin film structure in dark and under UV light. The Ti/Au contact on thin film is grounded.

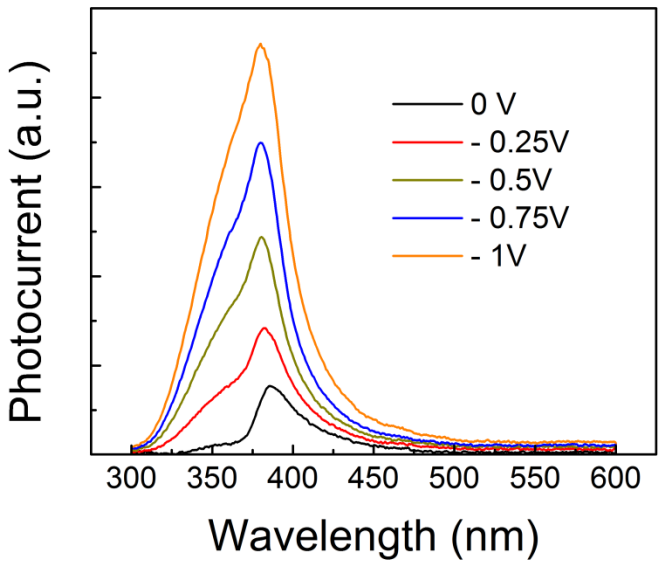

Figure 6.7. Photocurrent spectra under zero and reverse biases.

Figure 6.8 shows electroluminescence (EL) spectra of the device at different drive currents. At the drive current of 2 mA, only background noise is observed in the EL spectra. Weak EL emission shows up when the current is increases to 2.5 mA. The intensity of the spontaneous emission from around 370 nm to 410 nm increased at a higher current of 3 mA. At the same time several lasing peaks appear at 3 mA although they are relatively weak and broad. The lasing peaks become stronger and sharper with a linewith of ~1.5 nm at 3.5 mA drive current. More lasing peaks are observed at 4 mA. The spacing between the adjacent lasing peaks varies and the peak positions between different measurements are different. These results indicate that the lasing peaks in the EL spectra should be related to the random lasing instead of F-P lasing. As seen from the SEM images, the nanowires are slightly tilted, thus the DBR reflector and nanowires top facets are not parallel. Therefore the parallel reflectors for F-P laser do not exist in our device. The random lasing phenomena are related to random light scattering among the nanowires.

The output power of the device was measured using a Thorlabs PM100 Optical Power Meter and Figure 6.9 shows the result. The dash lines are the guide to the eye, showing the threshold current of ~ 3 mA. The integrated intensity of the EL spectra (Figure 6.9 inset) as a function of injection current also shows a threshold current at around 2.8 mA. The output power is about 220 nW at a drive current of 16 mA. The output power is much higher while the drive current is much lower than our previous device without DBR structure (40 mA threshold current and 70 nW output power at 70 mA under the same measurement setup) with same device size.

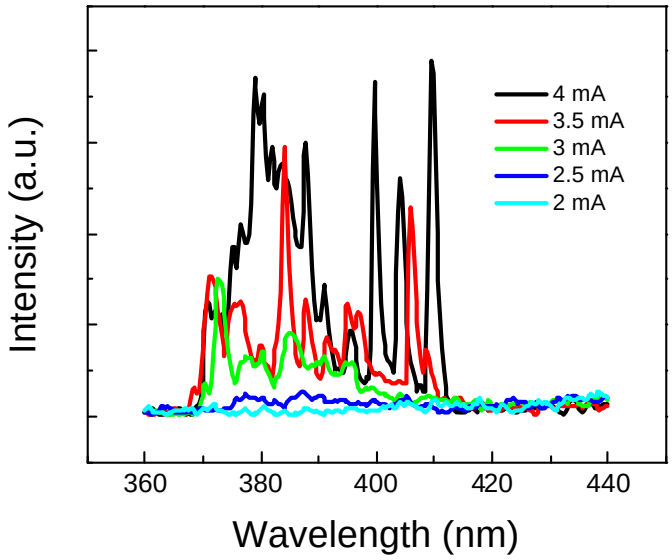

Figure 6.8. Lasing characterization of the device by electrical pumping. EL spectra of the laser device operated at the drive current from 2 mA to 4 mA.

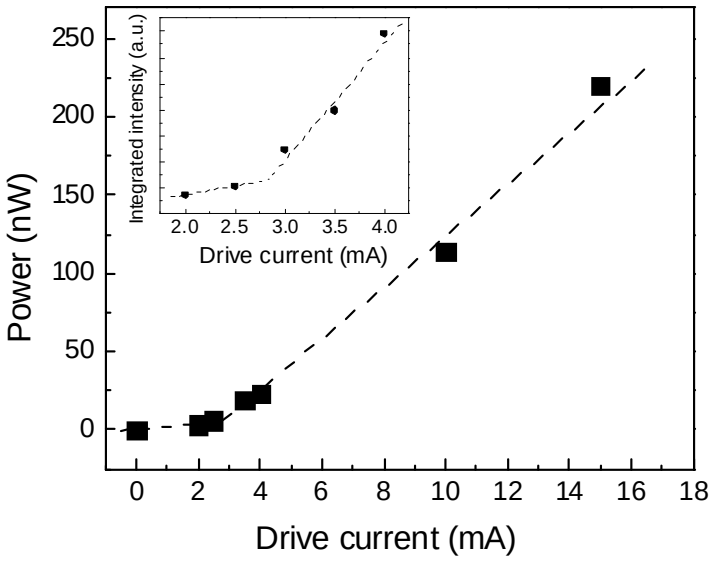

Figure 6.9. The output power as a function of drive current of the laser device. The inset is the integrated intensity of the EL spectra versus drive current. Both measurements show the threshold at around 3 mA.

For a random laser, different random cavities emit lasing signals in different directions due to random scattering. A detector placed at a certain angle to the sample can only collect lasing signals along the direction. In our measurement setup, the detector was placed at the normal direction to the sample surface. The enhanced signals should be related to the reflection from the DBR because the nanowires are slightly titled with respect to the normal of the substrate surface. In addition, the light initially emitted from the diode propagates all directions and a large portion is toward the substrate direction. In our previous device [7], the ideal reflectivity between ZnO and Si interface at around 380 nm is only around 20 %, and most of the light penetrates into the silicon and is absorbed by the substrate. Since the reflectivity of the DBR structure in the present device reaches 95 % at 380-390 nm, most of light will be reflected back to the ZnO nanowires/thin film structure, leading to more scattering among the nanowires. The threshold of a laser device is strongly related to the reflectivity and it can be reduced by increasing the reflective of the reflectors [17,18]. For both the devices with and without DBR, the reflectivity of the top ITO and ZnO interface are the same. The much lesser mirror loss from the DBR results in a lower threshold current and a higher output power.

6.4 Summary

In conclusion, the nitrogen doped p-type ZnO nanowires were grown on undoped n-type ZnO thin film on a 10-period DBR structure of alternative layers made from SiO_2 and SiN_x. The nitrogen doped nanowires were studied by XPS and low-temperature PL measurements. The p-n junction was confirmed by I-V and photocurrent characteristics.

The device showed strong random lasing emissions. The threshold current as low as 3 mA was achieved and the output power was also increased to be around 220 nW owing to the high reflectivity of the DBR.

References

[1] B. Redding, M. A. Choma, and H. Cao, *Nat. Photonics* **6**, 355 (2012).

[2] Q. Song, S. Xiao, Z. Xu, V. M. Shalaev, and Y. L. Kim, *Opt. Lett.* **35**, 2624 (2010).

[3] Q. Song, Z. Xu, S. H. Choi, X. Sun, S. Xiao, O. Akkus, and Y. L. Kim, *Biomed. Opt. Express* **1**, 1401 (2010).

[4] D. C. Look, *Mater. Sci. Eng. B* **80**, 383 (2001).

[5] M. H. Huang, S. Mao, H. Feick, H. Yan, Y. Wu, H. Kind, E. Weber, R. Russo, and P. Yang, *Science* **292**, 1897 (2001).

[6] S. Chu, G. Wang, W. Zhou, Y. Lin, L. Chernyak, J. Zhao, J. Kong, L. Li, J. Ren, and J. Liu, *Nat. Nanotechnol.* **6**, 506 (2011).

[7] J. Huang, S. Chu, J. Kong, L. Zhang, C. M. Schwarz, G. Wang, L. Chernyak, Z. Chen, and J. Liu, *Adv. Opt. Mater.* **1(2)**, 179 (2013).

[8] C. Y. Liu, H. Y. Xu, J. G. Ma, X. H. Li, X. T. Zhang, Y. C. Liu, and R. Mu, *Appl. Phys. Lett.* **99**, 063115 (2011).

[9] X. Ma, J. Pan, P. Chen, D. Li, H. Zhang, Y. Yang, and D. Yang, *Opt. Express* **17**, 14426 (2009).

[10] X. Y. Liu, C. X. Shan, S. P. Wang, Z. Z. Zhang, and D. Z. Shen, *Nanoscale* **4**, 2843 (2012).

[11] B. Ellis, M. A. Mayer, G. Shambat, T. Sarmiento, J. Harris, E. E. Haller, and J. Vučković, *Nat. Photonics* **5,** 297 (2011).

[12] H. Zhu, C. -X. Shan, B. -H. Li, Z. Z. Zhang, D. -Z. Shen, and K. -L. Choy, *J. Mater. Chem.* **21**, 2848 (2011).

[13] J. Rudolph, D. Hägele, H. M. Gibbs, G. Khitrova, and M. Oestreich, *Appl. Phys. Lett.* **82**, 4516 (2003).

[14] J. Y. Kong, S. Chu, J. Huang, M. Olmedo, W. H. Zhou, L. Zhang, Z. H. Chen, and J. L. Liu, *Appl. Phys. A* **110**, 23(2013).

[15] L. Liu, J. Xu, D. Wang, M. Jiang, S. Wang, B. Li, Z. Zhang, D. Zhao, C. -X. Shan, B. Yao, and D. Z. Shen, *Phys. Rev. Lett.* **108**, 215501 (2012).

[16] I. L. Krestnikov, N. A. Maleev, M. V. Maximov, A. F. Tsatsul'nikov, A. E. Zhukov, A. R. Kovsh, I. V. Kochnev, N. M. Shmidt, N. N. Ledentsov, V. M. Ustinov, P. S. Kop'ev, Zh. I. Alferov, and D. Bimberg, *Proceedings of the 7th International Symposium "Nanostructures: Physics and Technology"*, Ioffe Institute, St. Petersburg, Russia, June 14-18, p. 131 - 134 (1999).

[17] M. Oshikiri, H. Kawasaki, F.Koyama, and K.Iga, *IEEE Photon Technol Lett* 1, 11 (1989).

[18] G. M. Yang, M. H. MacDougal, and P. D. Dapkus, *IEEE Photon Technol Lett* **7**, 1228 (1995).

Chapter 7

Summary

1) ZnO is promising material for ultraviolet wide band gap nonvolatile memory devices and optoelectronic devices due to its outstanding properties. In this dissertation, based on the achievement of doped ZnO thin films and nanostructures, ZnO nonvolatile memories and random lasers are demonstrated and studied.

2) A ZnO p-n-p structure using Sb doped ZnO as p-type layer and undoped ZnO as n-type layer on c-plane sapphire substrate was demonstrated in Chapter 2. SIMS result showed good interface between Sb doped and undoped layers. The formation of p-n junction was proved by the good rectification I-V behavior between p-type layer and n-type layer. A hole concentration $N_A = 5.95 \times 10^{16}\ cm^{-3}$ was obtained from the fitting of the C-V curve by using small signal model, which cannot be done by Hall effect measurement. The nonvolatile memory effect of the p-n-p structure related to the charge storage in the n-layer of the p-n-p structure was also studied. The program and retention characteristics showed that ZnO p-n-p memory structure can achieve low operation voltage and long retention time, which suggests that the Sb doped p-type ZnO could be excellent material for future memory application.

3) ZnO n-p-n memory structure based on nanorods and thin film was also demonstrated. To achieve the n-p-n structure, homojunction nanorods are grown using Na as p-type dopant. First, vertically aligned Na-doped nanorods were grown on a ZnO seed layer on

Si via CVD at 700 ℃. The Na-doped nanorods were studied by the temperature-dependent photoluminescence and activation energy of ~200 meV was estimated. The p-type conductivity of the Na-doped nanorods was further confirmed by the output and transfer characteristics of the nanorod back-gated FET. Second, vertically aligned ZnO nanotips, nanotubes and nanorods were synthesized without catalytic assistance on the p-type Na-doped ZnO nanorods. The different morphology originates from different Zn vapor concentration. The n-p-n memory structure based on the homojunction nanorod and undoped seed layer was fabricated. The programming and retention characteristics show good memory effect and in turn, confirm the formation of the p-n homojunction nanorods. The demonstration of nanorod based n-p-n memory is a critical step to study the scalability of this memory. Furthermore, these diverse vertically aligned nanostructures on p-type ZnO nanorods are promising for future nanoelectronics and optoelectronic applications.

4) In chapter 4, current self-complianced and self-rectifying bipolar resistive switching was observed and studied in Ag-contacted, Na-doped ZnO nanowire resistive stwiching memory. SEM, HSR-AES and I-V characteristics show that the resistive switching was controlled by the formation and rupture of Ag nano-island chain on the surface of the nanowire. The self-compliance is induced by Na-doping and partial retraction of Ag from the nanoisland chain while the self-rectifying behavior is mainly originated from asymmetric contact between nanowire and Ag contact induced by Na-doping and Ag atom segregation and doping. The demonstration of current self-compliance and self rectifying in Na-doped nanowire resistive memory can significantly simplify the future

resistive swtiching random access memory circuitry because no separate selector device is necessary.

5) A homojunction random laser device based on nitrogen doped p-type nanowires and undoped n-type thin film was studied. P-type nitrogen doped ZnO nanowires were grown by using CVD without any metal catalyst on ZnO seed layer on silicon substrate. The p-type behavior was studied by the output characteristic and transfer characteristic of the nanowire back-gated FET and temperature dependent PL measurements. An acceptor activation energy of ~200meV was obtained from PL and carrier concentration statistics. The formation of the p-n junction was confirmed by I-V and EBIC results. The lasing behaviors were studied by using both optical pumping and electrical pumping methods. Above the threshold pumping power/current of 0.3 MW/cm^2 / 40 mA, random lasing actions featuring a series of lasing peaks in the spectra were observed. The output power of the electrically pumped laser was measured to be 70 nW at a drive current of 70 mA. The angle dependant EL result showed that the emission has a broad angle distribution, further indicating the formation of ZnO nanowires p-n homojunction random laser.

6) The DBR structure was utilized to improve the performance of the homojunction random laser devices. The nitrogen doped p-type ZnO nanowires were grown on undoped n-type ZnO thin film on a 10-period DBR structure of alternative layers made from SiO_2 and SiN_x on Si substrate. The nitrogen incorporated into the ZnO nanowires was confirmed by XPS spectrum and the p-type conductivity was studied by low-temperature PL measurement. The formation of homo p-n junction was confirmed by the I-V and

photocurrent characteristics. The random laser device showed strong random lasing emissions. The laser performance was improved owing to the DBR. The threshold current as low as 3 mA was achieved and the output power also was increased to be around 220 nW. The improvement of the laser performance should be due the high reflectivity of the DBR.

Acknowledgment

1) The results in Chapter 2 were published in "J. Huang, Z. L. Li, S. Chu, and J. L. Liu, Appl. Phys. Lett. **101**, 232102 (2012)".

(http://scitation.aip.org/content/aip/journal/apl/101/23/10.1063/1.4769097)

2) The results in Chapter 3 were published in "J. Huang, J. Qi, Z. L. Li, and J. L. Liu, Nanotechnology **24**, 395203 (2013)".

(http://iopscience.iop.org/0957-4484/24/39/395203/)

3) Most of the results in Chapter 4 were published in "J. Qi, J. Huang (Co-first author), D. Paul, J. J. Ren, S. Chu, and J. L. Liu, Nanoscale **5**, 2651(2013)" - Reproduced by permission of The Royal Society of Chemistry.

(http://pubs.rsc.org/en/content/articlelanding/2013/nr/c3nr00027c#!divAbstract)

4)Most of the results in Chapter 5 were published in "J. Huang, S. Chu, J. Y. Kong, L. Zhang, C. M. Schwarz, G. P. Wang, L. Chernyak, Z. H. Chen, and J. L. Liu, Advanced Optical Materials **1(2)**, 179 (2013)". Copyright Wiley-VCH Verlag GmbH & Co. KGaA. Reproduced with permission.

(http://onlinelibrary.wiley.com/doi/10.1002/adom.201200062/abstract)